

Insights into the mechanics of pure and bacteria-laden sessile whole blood droplet evaporation

Durbar Roy¹, Sophia M¹, Kush K Dewaangan¹, Abdur Rasheed¹,
Siddhant Jain¹, Anmol Singh², Dipshikha Chakravorty², and
Saptarshi Basu^{1†}

¹Department of Mechanical Engineering, Indian Institute of Science, Bengaluru, 560012, India

²Department of Microbiology and Cell Biology, Indian Institute of Science, Bengaluru, 560012, India

(Received xx; revised xx; accepted xx)

We study the mechanics of sessile blood drop evaporation using optical diagnostics, theoretical analysis, and micro/nano-characterization. The transient evaporation process has three major phases (A, B, and C) based on the evaporation rate. Phase A is the fastest, where edge evaporation dominates and forms a gelled three-phase contact line. Gelation results from sol-gel phase transition that occurs due to the accumulation of red blood cells, as they get transported due to outward capillary flow generated during drop evaporation. The intermediate phase B consists of a gelation front propagating radially inwards due to the combined effect of outward capillary flow and drop height reduction evaporating in pinned mode, forming a wet gel phase. We unearthed that the gelation of the entire droplet occurs in Phase B, and the gel formed contains trace amounts of water that are detectable in our experiments. Phase C is the final slowest stage of evaporation, where the wet gel transforms into a dry gel and leads to desiccation induced stress, forming diverse crack patterns in the dried blood drop precipitate. We observe radial and orthoradial cracks in the precipitate's thicker region, mud-flat cracks in the drop center, and the outer contact line where thickness and curvature are relatively small. We also study the evaporation of bacteria-laden droplets to simulate bacterial infection in human blood and show that the drop evaporation rate and final dried residue pattern do not change appreciably within the parameter variation of the bacterial concentration typically found in bacterial infection of living organisms.

Key words: Authors should not enter keywords on the manuscript, as these must be chosen by the author during the online submission process and will then be added during the typesetting process (see <http://journals.cambridge.org/data/relatedlink/jfm-keywords.pdf> for the full list)

1. Introduction

In this study, we investigate the mechanics of sessile blood droplet evaporation. Understanding the behavior of blood droplet evaporation is essential in forensic science, biotechnology, and the development of advanced medical diagnostics (Chen *et al.* 2016;

† Email address for correspondence: sbasu@iisc.ac.in

Cameron *et al.* 2018; Kokornaczyk *et al.* 2021; Pal *et al.* 2023; Demir *et al.* 2024). We also observe evaporation in various biological and bodily fluids like blood clots, desiccation in wounds (Sobac & Brutin 2011; Brutin *et al.* 2011; Laux *et al.* 2016), biofilm formations (Wilking *et al.* 2013), and drying of tears (Traipe-Castro *et al.* 2014) to name a few that are found in living systems. Apart from forensics and disease diagnostics, analysis of desiccated biological samples is essential in several applications like archaeological studies (Wilson *et al.* 2013), micro-array applications for proteins, nucleic acids (DNA, RNA), genotype and phenotype studies (Smalyukh *et al.* 2006). Analyzing the characteristics of sessile blood droplets during and after evaporation can provide valuable insights into the blood sample's source, age, and composition. The physics of sessile blood drop evaporation falls at the intersection of various disciplines like fluid mechanics, solid mechanics, soft matter, statistical physics, surface chemistry, colloidal physics, and biology, to name a few (Brutin 2015). Quantitative understanding of blood droplet evaporation and its corresponding precipitate formation mechanics still remains in its infancy (Lanotte *et al.* 2017).

Blood is a complex fluid consisting of formed cellular elements suspended in blood plasma (Baskurt & Meiselman 2003; Hoffbrand & Steensma 2019). Various cellular elements like erythrocytes (red blood cells (RBCs)), leukocytes (white blood cells (WBCs)) and thrombocytes (platelets) form approximately 45-50% of the blood volume, with RBCs having the most significant percentage among the cellular elements. On the other hand, blood plasma is an amber color liquid component of the blood, which makes approximately 50-55% of the total blood volume. 94-95% of the blood plasma by volume is essentially water, with the remaining 5-6% being dissolved proteins, electrolytes, glucose, clotting factors, hormones, carbon dioxide, and oxygen. We can, therefore, approximate blood as a colloidal suspension (Israelachvili 2011) of RBCs in plasma, to first-order accuracy. The morphology of dried residues of blood drops hence depends primarily on the deposition of RBCs, the major solute component of blood plasma. However, other cellular components of blood (leukocytes and thrombocytes), dissolved proteins, electrolytes, hormones, and gases have a secondary role in the dried residue pattern formation. Such secondary effects are essential in developing diagnostic solutions for particular diseases in general (Kokornaczyk *et al.* 2021). However, in this work, we focus primarily on the deposit pattern caused by RBCs.

Evaporation of biofluids like blood, saliva, mucus, and urine has been explored majorly in sessile droplet and thin film configurations on solid substrates due to the simplicity of the experimental setup (Hu & Larson 2002, 2005; Brutin 2015; Kokornaczyk *et al.* 2021; Wilson & D'Ambrosio 2023). The major observations for sessile blood droplet evaporation were the formation of a ring-like deposit at the contact line and a complex set of crack patterns in the desiccated drops and films. The different patterns formed in evaporating drops and films of biological fluids resembled patterns found in various colloidal systems hinting towards some unifying underlying laws that were common to biofluids, colloids, and pure fluids in general (Deegan *et al.* 1997, 2000; Dufresne *et al.* 2003; Allain & Limat 1995; Tarasevich *et al.* 2011; Denkov *et al.* 1992; Adachi *et al.* 1995). Previous studies by scientists and engineers using model fluids like mucin revealed that both deposition and crack formation depends strongly on the particle concentration and types of dissolved salts, macro-molecules, proteins, and surfactants (Nguyen & Stebe 2002). This work explores blood drop evaporation physics in depth and also tests whether microbial bacteria present in blood simulating bacterial infection found in living organisms can affect the evaporation process and the resulting dried precipitate.

Various kinds of optical diagnostics methods are used to study complex biological fluids in different conditions. It has been shown by various research groups (Yakhno *et al.*

2005; Shatokhina *et al.* 2004; Esmonde-White *et al.* 2014; Kokornaczyk *et al.* 2021) that pathological changes of solute and solvent composition affect the morphology of the dried residues in evaporating drops and films. Up to the recent decade, desiccation studies on biological fluids have majorly focused on solutions, but the evaporation physics of drying suspensions is relatively sparse. The seminal work of Brutin *et al.* (Brutin *et al.* 2011) and Chen *et al.* (Chen *et al.* 2016) is an exception. Blood is a concentrated colloidal suspension with particle volume fraction / Hematocrit (Ht) of $Ht \sim 40 - 45\%$ in the physiological range of healthy individuals (Reinhart 2016). Based on volume ratio, blood can be thought of comprising of two major components, RBCs ($V_{RBCs}/V \sim 40 - 45\%$) and plasma ($V_{plasma}/V \sim 60 - 55\%$) where V_{RBCs} , V_{plasma} represents the respective volumes in a total blood volume of V . Plasma is the protein (fibrinogen, albumin) laden aqueous salt solution suspending medium for the micron-size deformable RBCs in the corpuscular phase. RBCs are typically biconcave shape at rest. The very high concentration of RBCs makes visualization of evaporating blood droplets challenging in general. Brutin and his collaborators analyzed blood drop evaporation using optical diagnostics and mass measurements. The droplet evaporation mechanism, desiccation time, and morphology of dried blood residues were unearthed by Brutin *et al.* (Brutin *et al.* 2011) using experimental techniques. However, a comprehensive quantitative model of the various processes that occur during blood drop evaporation is relatively unexplored in detail.

This work fills some of the research gaps using experimental and theoretical techniques to understand the underlying fundamental processes that occur during blood drop evaporation. In general, the evaporation and the dried residue of a desiccating biological fluid such as blood depend on the ambient environmental factors (like temperature and humidity), substrate characteristics (like chemical composition, wettability, adhesion), droplet geometry, fluid mechanical (like density, viscosity, surface tension, pathology), physicochemical, thermofluidic, and biophysical properties. The dried blood drop dominant pattern consists of a thick rim called a corona and a center region of relatively small thickness. The coronal rim thickness is caused due to the transport of RBCs by capillary flow induced by sessile drop evaporation. The interaction of desiccation induced stress and thickness variation from the drop center to the outer rim region in the radial direction causes crack patterns of different morphologies. Radial cracks are formed in the rim region, whereas mud-flat cracks are formed in the center and outer periphery of the dried residues. Evaporating colloidal and polymeric sessile drops analogously form a skin layer at the air-liquid interface, which eventually undergoes a buckling. Current literature on blood drop evaporation is primarily based on observational characteristics of drop shape, mass, and crack patterns (Hertaeg *et al.* 2021; Choi *et al.* 2020; Mukhopadhyay *et al.* 2020; Iqbal *et al.* 2020; Bahmani *et al.* 2017). However, a fundamental mechanistic understanding of the blood drop desiccation process is far from complete and requires thorough quantitative analysis. This work serves as a bridge to understanding the mechanics of blood drop evaporation using ideas from colloidal desiccating drops. We decipher the various phases and the allied mechanisms of blood drop drying using high-fidelity color optical imaging, quantitative theoretical modeling, and experimental micro/nano-characterization. It is important to note that the current work establishes the mechanics of the various processes and phases related to blood droplet drying physics in a quantitative manner using experimental and theoretical methods. However, detailed characterization for all experimental parameter regimes and a full-scale numerical simulation of the various processes involved is beyond the scope of the present work.

The current manuscript is structured as follows. Section 2 discusses the materials and methods in several subsections. Blood sample preparation, experimental setup, and

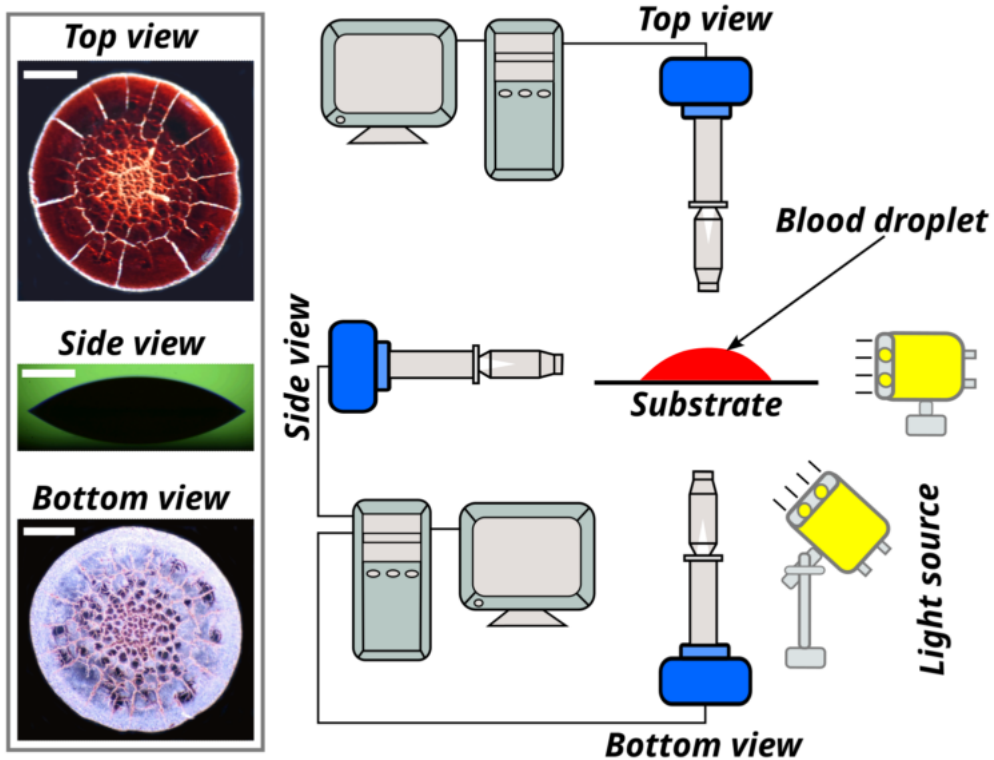


FIGURE 1. Schematic of the experimental set up and sample top, side and bottom view images of dried blood drop precipitate. Scale bar depicted in white represents 1 mm.

dried residue characterization are discussed in sections 2.1, 2.2, and 2.3, respectively. Section 3.1 introduces the key results as a global overview. Section 3.2 discusses the coordinate system and sessile droplet evaporation physics. Section 3.3 discusses the various stages of blood drop evaporation. Section 3.4 discusses the quantitative modeling and the generalized mechanics of blood drop evaporation. Section 3.5 presents the characterization of dried blood residues and discusses the cracking mechanics due to desiccation stresses. Section 4 concludes the manuscript.

2. Materials and Methods

2.1. Blood sample preparation

Blood samples were collected from three healthy volunteers (one female and two male) in the age group (25-40 years) with proper consent. 10 ml of whole blood was drawn in K3-EDTA (tripotassium Ethylene Diamine Tetraacetic Acid) vacutainer containers to prevent the blood from clotting. 2-4 ml of the collected blood were sent for several blood tests (CBC (Complete Blood Count), PT (Prothrombin Time), and ESR (Erythrocyte Sedimentation Rate) (refer to supplementary table ST1 for relevant blood report data)) relevant to the mechanics of the various processes that occur during evaporation. Overnight grown stationary phase cultures of *Klebsiella pneumoniae* MH1698 were taken, and their absorbance was measured at OD600nm. Various bacterial concentrations in the range of $\mathcal{O}(10 - 10^9)$ CFU/mL of the bacterial culture were pelleted down at 6000

rpm for 6 minutes. CFU (colony forming units) is a measure of the number number of viable microbial cells in a sample. The pellets were washed twice with phosphate-buffered saline (PBS) pH 7.4 and resuspended in 500 μL EDTA whole blood. For confocal microscopy studies, *S. Typhimurium* expressing Green Fluorescent Protein (GFP) (pFV-GFP) (STM-GFP) strains were used.

2.2. Experimental setup

Figure 1 shows a schematic representation of the experimental setup. The experimental setup consists of a blood drop evaporating on a clean glass slide of dimensions $75 \times 25 \times 1 \text{ mm}^3$ (procured from Blue Star). Blood droplet with a volume of $3.4 \pm 0.8 \mu\text{L}$ was placed gently on the glass slide using a micro-pipette. All the evaporation experiments were performed at a relative humidity (RH) of $45 \pm 3\%$ and an ambient temperature of $25 \pm 2^\circ\text{C}$ measured using a TSP-01 sensor, Thorlabs. The complete evaporation process is recorded using color optical diagnostics from three views, i.e., top, side, and bottom. The top and bottom views were operated in reflection mode, whereas shadowgraphy was performed using side-view imaging. Color images of the corresponding views (top, bottom, and side) were recorded using 3 DSLR cameras with an image resolution of 24 megapixels (Nikon D5600) coupled with Navitar zoom lens assembly (2X lens \times 4X adapter tube). A 5W LED light source (Holmarc) and a 50W mercury lamp were used to provide uniform illumination for the three imaging views. A spatial resolution of $1 \mu\text{m}/\text{pixel}$ was used for the optical color imaging. Consecutive images were captured at a time delay of 10 seconds. Typical sample top, side, and bottom view images are shown in figure 1 respectively (refer to supplementary movies for temporal data of drop evaporation). The scale bar in white denotes 1mm. The instantaneous geometrical parameters and features (shape descriptors) are extracted using image processing techniques applied to the side, top, and bottom view images using open source software ImageJ (Schneider *et al.* 2012) and python programming language (Van Rossum & Drake 2009).

2.3. Dried residue characterization

Scanning Electron Microscopy (SEM) was employed to analyze the surface characteristics of the deposits, revealing the microcrack patterns through high-resolution imaging. Ultra55 FE- SEM Karl Zeiss EDS instrument is used. SEM images showed the detailed crack patterns and stacking of RBCs on the surface. Before the SEM examination, the deposit surfaces were desiccated for 24 hours and then coated with a thin layer of gold, approximately 10 nm thick, to facilitate SEM and profilometric studies. A non-contact optical profilometry method was utilized to assess the deposit's geometrical features. The measurements were conducted using a Taylor Hobson 3D surface and film thickness optical profiler. Additionally, the TalySurf CCI, a commercial optical metrology software, was used to process the data. Zeiss LSM 880 NLO upright multi-photon confocal microscope was used to image the dried sessile blood droplet precipitate at 10X magnification. ZEN Black software (Carl Zeiss) was used to obtain the Z stack images to study the bacterial deposition in the precipitates.

3. Results and Discussions

3.1. Global overview

In this work, we study the mechanics of sessile blood drop evaporation (figure 2) using EDTA-based pure and bacteria-laden whole blood with varying levels of bacterial concentration typically found in living organisms theoretically and experimentally

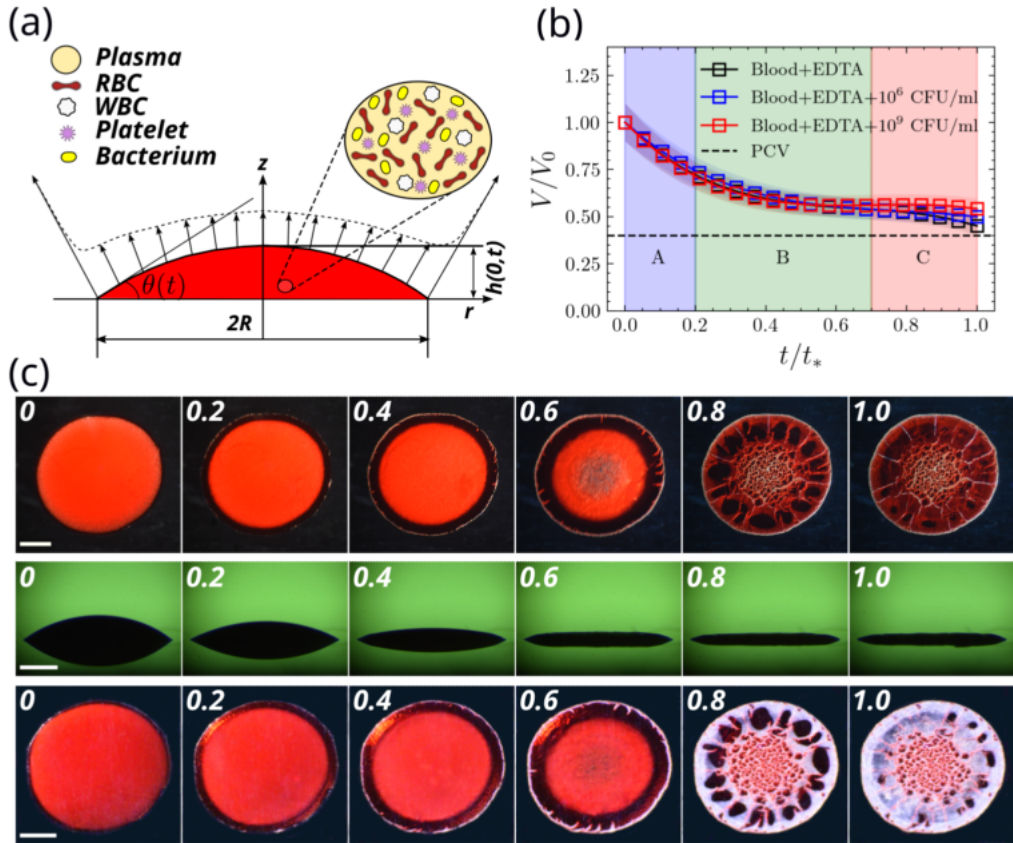


FIGURE 2. (a) Schematic of the coordinate system, composition of the blood and initial condition of sessile blood drop evaporation. (b) Non dimensional volume (V/V_0) regression plotted as a function of non dimensional time (t/t_*) for whole blood + EDTA, whole blood + EDTA + 10^6 CFU/ml KP (Klebsiella pneumoniae) bacteria and whole blood + EDTA + 10^9 CFU/ml KP bacteria respectively. The different phases of sessile blood drop evaporation depicted as A, B and C respectively. (c) Top view, side view and bottom view time sequence images of the evaporation process respectively. Scale bar for the top, side and bottom view represents 1 mm respectively. The timestamps are in non dimensional units (t/t_*).

using lubrication theory, color optical imaging, and micro/nano-characterization. Figure 2(a) depicts the schematic representation of an evaporating sessile droplet. Figure 2(b) represents the normalized volume regression of the evaporating droplet for various blood samples (pure and bacteria-laden). We observe that the volume regression is independent of the bacterial concentration range typically found in living organisms. The normalized volume asymptotes the packed cell volume (PCV) of the blood sample at the end of evaporation. We further observe from figure 2 (b) that the transient evaporation process can be subdivided into three phases (A, B, and C) based on the evaporation rate. Figure 2(c) represents the top, side, and bottom view image sequences of the evaporation process. Phase A (figure 2(b,c): $t/t_* = 0-0.2$) is the fastest where edge evaporation dominates and leads to the formation of a gelation three-phase contact line front propagating radially inwards. Here t denotes the instantaneous time and t_* denotes the total evaporation time scale comprising of all the three phases. The radially outward capillary flow generated by drop evaporation causes the RBCs to accumulate at the outer edge of the droplet.

The intermediate phase B (figure 2(b,c): $t/t_* = 0.2 - 0.7$) consists of gelation of the entire droplet due to the radially inward propagating gelation front and the simultaneous reduction of droplet height $h(r, t)$ and contact angle $\theta(t)$ (refer to figure 2(a) for the various shape descriptors of a sessile droplet). The radially inward propagating gelation front leads to RBC deposition, causing the formation of a thick rim around the droplet periphery known as corona (Brutin *et al.* 2011). Gelation in phases A and B occurs due to the sol-gel phase transition. The sol-gel phase transition occurs when the solute concentration (RBCs here) becomes larger than a critical concentration. We unearth that the gelation of the entire droplet occurs in Phase B. At the end of Phase B, the gel formed contains some trace amount of water. The trace amount of water makes the gel wet and stick (laminated) to the glass substrate due to the hydrophilic nature of the glass. Phase C (figure 2(b,c): $t/t_* = 0.7 - 1.0$) is the final slowest stage of evaporation, where the wet gel formed during Phase A and Phase B transforms into dry gel due to a very slow evaporation process. Due to the continued loss of water from the wet gel, the laminated regions adhered to the glass substrates undergo delamination. On further desiccation, the drying droplet results in high azimuthal stress, forming radial cracks in the corona region. Mudflat cracks are observed in the center part of the evaporating droplet, where the drop thickness is relatively small and curvature is negligible. We further show that the drop evaporation rate and the corresponding dried residue pattern do not change appreciably within the parameter variation of the bacterial concentration typically found in living organisms (figure 2(b)).

3.2. Coordinate system and sessile droplet evaporation physics

Figure 2(a) shows the schematic of the evaporating droplet and the associated coordinate system. An axisymmetric cylindrical coordinate system ($r-z$) is used to describe and analyze the evaporation process quantitatively. Here, r represents the radial coordinate, and z represents the axial coordinate, the vertical axis along which the droplet liquid-vapor interface profile would be symmetric. In general the sessile droplet can be described by certain geometrical shape descriptors like contact angle (θ), contact radius (R), and drop central height ($h(0, t)$) for a particular initial droplet volume and substrate. For small Bond number ($Bo = \Delta\rho g l^2 / \sigma < 1$), the droplet geometry can be approximated by a spherical cap geometry (Hu & Larson 2002; Gennes *et al.* 2004; Clift *et al.* 2005), where $\Delta\rho$ is the density difference at the liquid air interface, g is the acceleration due to gravity, l is the characteristic length scale, and σ is the liquid air surface tension. For the current experiments, using $\Delta\rho \sim \mathcal{O}(10^3)$ kg/m³, $g \sim \mathcal{O}(10)$ m/s², $l \sim R \sim \mathcal{O}(10^{-3})$ m, and $\sigma \sim \mathcal{O}(7 \times 10^{-2})$ N/m, we have $Bo \sim \mathcal{O}(10^{-1}) < 1$ and hence spherical cap assumption can be used to describe the evaporating droplet. The interface profile of the sessile droplet is therefore given by (Hu & Larson 2002)

$$h(r, t) = \sqrt{\frac{R^2}{\sin^2 \theta} - r^2} - \frac{R}{\tan \theta} \quad (3.1)$$

and the corresponding drop volume is given by

$$V(t) = \pi h(0, t)[3R^2 + h^2(0, t)]/6 \quad (3.2)$$

where $h(0, t) = R \tan(\theta(t)/2)$. In case of blood drop evaporation, the spherical cap assumption would be valid upto a particular time scale ($t/t_* \sim 0.5$) after which deviation from spherical cap geometry becomes too large due to the effect of gelation. Initially (i.e., $t/t_* = 0$), the evaporative flux profile at the drop interface is highest at the drop contact line and least at the drop center (refer to figure 2(a)). Diffusion-limited evaporation model can be used to approximate isothermal sessile drop evaporation for thin droplets in the

size range of mm (i.e., $R \sim \mathcal{O}(10^{-3})\text{m}$ and $h < R$) to a very high degree of accuracy. The size where molecular reaction kinetics dominates diffusion evaporation phenomena occurs approximately at length scales of the order of 100nm (Agharkar *et al.* 2024), which is considerably very small with respect to the typical length scale that we have in our current experiments, therefore conforming to diffusion-limited drop evaporation. Drop evaporation, in general, can occur in various modes like CCR (constant contact radius) and CCA (constant contact angle) (Wilson & D'Ambrosio 2023) depending on the wettability of the substrate. For hydrophilic substrates with an initial acute contact angle, as is the present case, drop evaporation generally occurs in the CCR mode of evaporation. In the CCR mode of evaporation, the droplet's three-phase contact line is pinned throughout the evaporation process while the contact angle decreases with time. For the present case of evaporating whole blood droplets, the evaporation occurs in CCR mode, as can be observed from the image snapshots in figure 2(c). The evaporation in CCR mode generates an capillary flow inside the droplet. For thin droplets the conservation of mass for the solvent in the evaporating droplet (water in general) is given by (Wilson & D'Ambrosio 2023)

$$\frac{\partial h}{\partial t} + \frac{1}{r} \frac{\partial(rh \langle u \rangle)}{\partial r} = -\frac{J}{\rho} \quad (3.3)$$

where $\langle u \rangle$ is the height average radial velocity, ρ is the liquid density and the evaporation flux J is given by

$$J = \frac{2Dc_v(1 - RH)}{\pi\sqrt{R^2 - r^2}} \quad (3.4)$$

for $0 \leq r < R$, where D is the diffusivity of water vapor in air, c_v is the saturation concentration of water vapor at the droplet interface at a particular temperature, and RH is the relative humidity. Using equation (3.4) in equation (3.3), the height averaged radial velocity can be computed as

$$\langle u \rangle = \frac{4Dc_v(1 - RH)}{\pi\rho\theta r} \left[1 - \left(1 - \frac{r^2}{R^2} \right)^{3/2} \right] \left(1 - \frac{r^2}{R^2} \right)^{-1/2} \quad (3.5)$$

where $(r, \theta) \neq 0$. For particle laden droplets the radially outward capillary flow can cause edge deposition like the coffee ring effect (Deegan *et al.* 1997). For dilute concentration of particles and assuming negligible particle diffusion the height averaged particle concentration $\langle c \rangle$ would satisfy

$$\frac{\partial \langle c \rangle}{\partial t} + \langle u \rangle \frac{\partial \langle c \rangle}{\partial r} = \frac{J \langle c \rangle}{\rho h} \quad (3.6)$$

Using equation (3.4), (3.5) and the method of characteristics for solving the first order PDE for $\langle c \rangle$ we have

$$\langle c \rangle = \langle c \rangle_0 \left[\left(\frac{\theta}{\theta_0} \right)^{-3/4} + \left(1 - \frac{r^2}{R^2} \right)^{3/2} - 1 \right]^{1/3} \left(1 - \frac{r^2}{R^2} \right)^{-1/2} \quad (3.7)$$

where $\langle c \rangle_0 = \langle c \rangle_0(r)$ is the initial depth average radial concentration field along the droplet radius. It is important to note that the average concentration computed from equation (3.7) is only valid for thin droplets and dilute solution. The variation of evaporation flux, depth average radial velocity and depth average particle concentration as a function of radial coordinate is shown in figure S1-S3 of the supplementary material respectively. It is important to note that the radial variation of evaporation flux, velocity

and particle concentration from equation (3.4, 3.5, and 3.7) is a monotonically increasing function. Further from equation (3.4, 3.5, 3.7) we can observe the singularity at the contact line $r = R$. For thin drops and dilute concentration the evaporative flux is independent of the height profile and the particle concentration, unlike blood drop evaporation where the dependence exists. For blood droplet evaporation the solution for J , h and $\langle c \rangle$ can not be obtained independently as depicted above and has to be obtained in a coupled manner (refer to section 3.4 for the details). This is due to the non-monotonic nature of the evaporation flux due to gelation. Further the non-trivial coupling between $\langle c \rangle$, J and h also plays an important role as discussed in later portion of the text (refer to section 3.4). From figure 2(b), we can observe that the entire CCR mode of the evaporation process can be further subdivided into three phases, A, B, and C, based on the descending rate of evaporation. Figure 2(b) represents the graph of normalized volume ratio (V/V_0) with normalized time (t/t_*) for the evaporating drop. Here V denotes the instantaneous drop volume, and V_0 denotes the initial drop volume. Here, t denotes the instantaneous time, and t_* denotes the complete evaporation time scale (defined experimentally as the time instant where no significant changes are observed in drop morphologies in all three views). From figure 2(b,c), we can observe that phase A corresponds to $t/t_* = 0 - 0.2$, phase B corresponds to $t/t_* = 0.2 - 0.7$ and phase C corresponds to $t/t_* = 0.7 - 1.0$. The mechanics of the individual phases during drop evaporation are discussed below.

3.3. Stages of blood drop evaporation

3.3.1. Phase A

Figure 3 shows the schematic representation of various processes that occur during Phase A. Figure 2(a) and 3(a) show the initial configuration of the evaporating blood droplet. The sample blood droplet is a suspension of cellular elements like RBCs, WBCs, platelets, and bacteria (for bacteria-laden drops) suspended in plasma. However, due to the very high number density of RBCs, blood can be approximated as a binary suspension to first approximation. Blood droplet evaporation on hydrophilic substrates occurs in CCR mode with a constant contact radius R due to the pinning of the contact line. For small drops, the droplet shape at the initial time can be approximated by a spherical cap. The evaporation flux along the droplet interface monotonically increases with radial coordinate r and peaks at the contact line at $t/t_* = 0$. The non-uniform evaporation flux along the drop interface generates a radially outward capillary flow that causes the RBCs to be transported towards the contact line. Figure 3(b,c,d) shows the magnified view near the contact line at $t/t_* = 0, 0.1, 0.2$ respectively. At the initial time of drop evaporation, a very thin precursor film of plasma exists at the outer edge of the droplet, which slowly solidifies (depicted schematically as red filled circles in figure 3(c) and 3(d)). The precursor film is devoid of RBCs as the dimension of the precursor film is smaller than a single RBC length scale. The outer radial capillary flow (shown in the blue arrow) causes the RBCs to accumulate, forming a gel phase. After the initial gelation of the three-phase contact line, a gelation front radially propagating inward is observed (vertical blue line in 3(c,d)). Further, the concentration of RBCs increases at the outer periphery, reducing evaporation flux at the drop interface near the contact line. A small dotted circle representing a control volume (CV) near the contact line is shown in figure 3(b). Figure 3(e) shows the zoomed-in view of the CV. The blood suspension inside the CV is initially in the sol phase. However, due to the outward capillary flow, the concentration of RBCs inside the control volume increases, leading to a phase transition that forms a wet gel phase. The evaporative flux over the wet gel

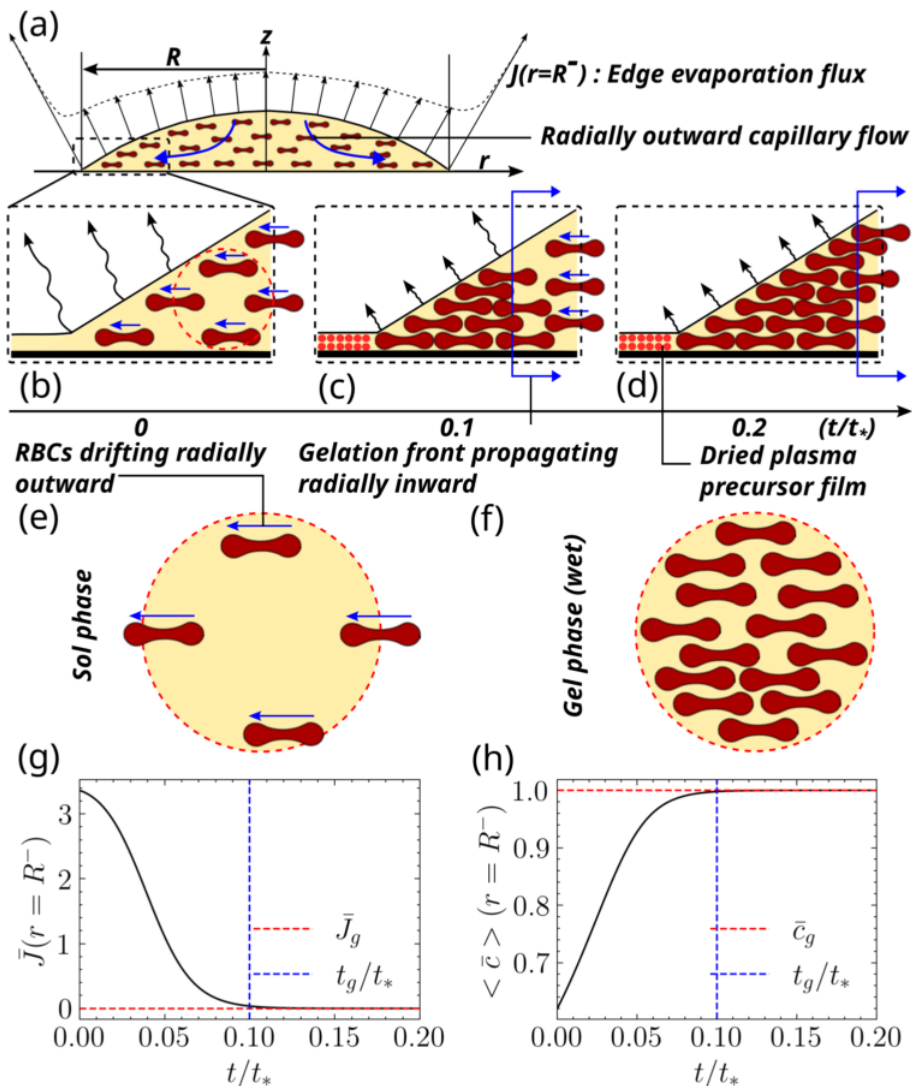


FIGURE 3. Schematic representation of the various processes occurring in Phase A of blood droplet evaporation. (a) Initial configuration of the sessile blood droplet at $t/t^* = 0$ depicting the evaporative flux and the radial outward capillary flow inside the evaporating droplet. (b,c,d) Magnified view of the outer edge of the droplet depicting the precursor film and the outward transport of RBCs towards the edge at (b) $t/t^* = 0$, (c) $t/t^* = 0.1$, and (d) $t/t^* = 0.2$ respectively. The blue vertical line shows the gelation front propagating radially inwards. (e) A small control volume (CV) near the three phase contact line depicting the sol phase in which RBCs are present inside the CV and getting transported across the surface of the CV. (f) Wet gel phase in the CV as RBCs concentration increases. (g) Non-dimensional evaporative flux variation depicting the decrease of evaporative flux at the outer edge of the droplet as a function of non-dimensional time due to RBCs accumulation. (h) Time evolution of the average concentration inside the CV depicting the sol-gel phase transition mechanism.

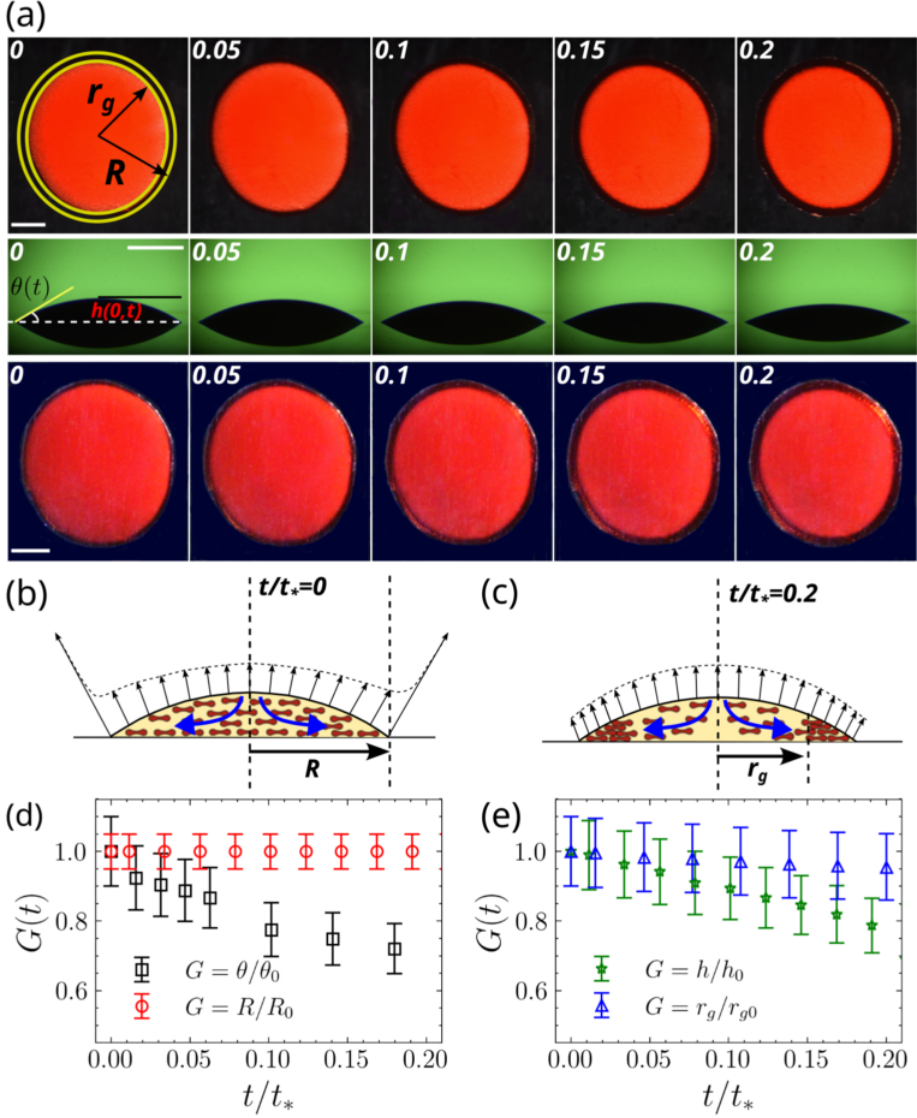


FIGURE 4. (a) Top, side and bottom view time sequence images of Phase A at different non dimensional time instants $t/t_* = 0, 0.05, 0.1, 0.15, 0.2$ respectively. Scale bar for top, side and bottom view represents 1.2 mm, 1.3 mm and 1 mm respectively. (b) Schematic representing the initial configuration of the evaporating droplet ($t/t_* = 0$). (c) Schematic representing the evaporating droplet at the end of evaporation phase A ($t/t_* = 0.2$) (d,e) Non dimensional geometrical drop parameters $G(t)$ (normalized contact angle (θ/θ_0), normalized contact radius (R/R_0), normalized drop height (h/h_0), and normalized gelation radius (r_g/r_{g0})) evolution as a function of non dimensional time t/t_* .

region reduces significantly as depicted in the schematic by the reduction of the length of the squigly black arrows depicting evaporative flux. Figure 3(g) shows the reduction of the non-dimensional evaporation flux \bar{J} at radial location $r = R^-$ (immediate inward vicinity of the contact line) as a function of non-dimensional time t/t_* (refer to section 3.4 for normalization of J). \bar{J}_g in figure 3(g) represents the reduced evaporative flux on the top of the gelled region of the droplet. Figure 3(h) shows the corresponding

rise in for depth average normalized RBCs concentration $\langle \bar{c} \rangle$ at $r = R^-$ due to the radially outward movement of RBCs caused by the capillary flow generated due to CCR mode of drop evaporation. Sol-gel transition occurs at the three-phase contact line as the concentration approaches a critical gelation concentration c_g (i.e., $\bar{c}_g = 1$). It is important to note that the average concentration of RBCs $\langle c \rangle$ is normalized to a non-dimensional concentration $\langle \bar{c} \rangle$ using the gelation concentration as the base (i.e., $\langle \bar{c} \rangle = \langle c \rangle / c_g$). It is important to note that the reduction of \bar{J} and the increase of $\langle \bar{c} \rangle$ signifying the sol-gel transition occurs at $t/t_* = 0.1$ (midway in phase A) as shown in figure 3(g) and 3(h). The plots in figure 3(g) and 3(h) are calculated using the coupled model discussed in section 3.4. Figure 4(a) shows the top, side, and bottom image sequence for Phase A of the evaporating blood droplet in the top, middle, and bottom panels, respectively. The constant contact pinned radius is denoted by R and the gelation radius by r_g . The drop contact angle is represented by θ , and the drop center height by $h = h(0, t)$. Figure 4(b,c) shows the schematic representation of the evaporation phase A at $t/t_* = 0$ and $t/t_* = 0.2$, respectively. Note the increase in concentration of RBCs and the corresponding reduction of evaporation flux in figure 4(c). Figure 4(d) shows the evolution of various normalized geometrical parameters $G(t)$ like normalized contact angle (θ/θ_0) and normalized contact radius (R/R_0) confirming CCR mode of drop evaporation. Figure 4(e) also shows the evolution of other normalized geometrical parameters like normalized droplet center height (h/h_0) and normalized gelation radius (r_g/r_{g0}) during phase A. It can be observed that the droplet height reduction is faster than that of the gelation front propagation. The faster reduction of central height is one of the important causes of the distinct dried droplet residue profile formed in phase C, which will be discussed later in the text.

3.3.2. Phase B

Phase B of the evaporation process spans from $t/t_* = 0.2 - 0.7$ and has the longest duration. In this phase, the gelation front propagates further radially inwards. As the droplet evaporates in CCR mode, the contact line is pinned, but the droplet contact angle and its corresponding maximum height decreases monotonically. As the droplet evaporates, the outward capillary flow causes a depletion of RBCs in the center, allowing the droplet interface to change its curvature smoothly. Figure 5 shows a schematic representation of the various processes occurring during phase B of evaporation. Figure 5(a) shows a 3D schematic of the evaporation process in phase B at $t/t_* = 0.3, 0.5, 0.7$. Figure 5(b) shows a magnified view of the droplet interface undergoing monotonic curvature (k) change from $k < 0$ to $k = 0$, to $k > 0$ at $t/t_* < 0.5$, $t/t_* \sim 0.5 - 0.6$, and $t/t_* > 0.6$ respectively. The corresponding side-view images are also shown. Figure 5(c) represents the corresponding top and bottom view images. Figure 6(a) shows the top, side, and bottom view image sequence during phase B of evaporation. The timestamps are normalized time (t/t_*). Figure 6(b) shows the droplet nondimensional geometrical parameters $G(t)$ evolution as a function of normalized time. Various parameters like normalized contact angle (θ/θ_0), normalized height h/h_0 , normalized contact radius (R/R_0), and normalized gelation radius (r_g/r_{g0}) is plotted in black, green, red, and blue respectively. It is important to note that at approximately ($t/t_* \sim 0.5 - 0.6$) there is a significant reduction of the droplet height compared to its contact angle signifying the deviation of the droplet shape from spherical cap approximation. Figure 6(c) shows a schematic representation of the starting ($t/t_* = 0.2$) and ending state ($t/t_* \sim 0.67 - 0.7$) of phase B, respectively. R denotes the contact radius and r_g denotes the gelation front radius. Notably, the distinct color change in the top view at the end of phase B ($t/t_* = 0.67$) signifies the completion of the gelation of the entire droplet. At the end

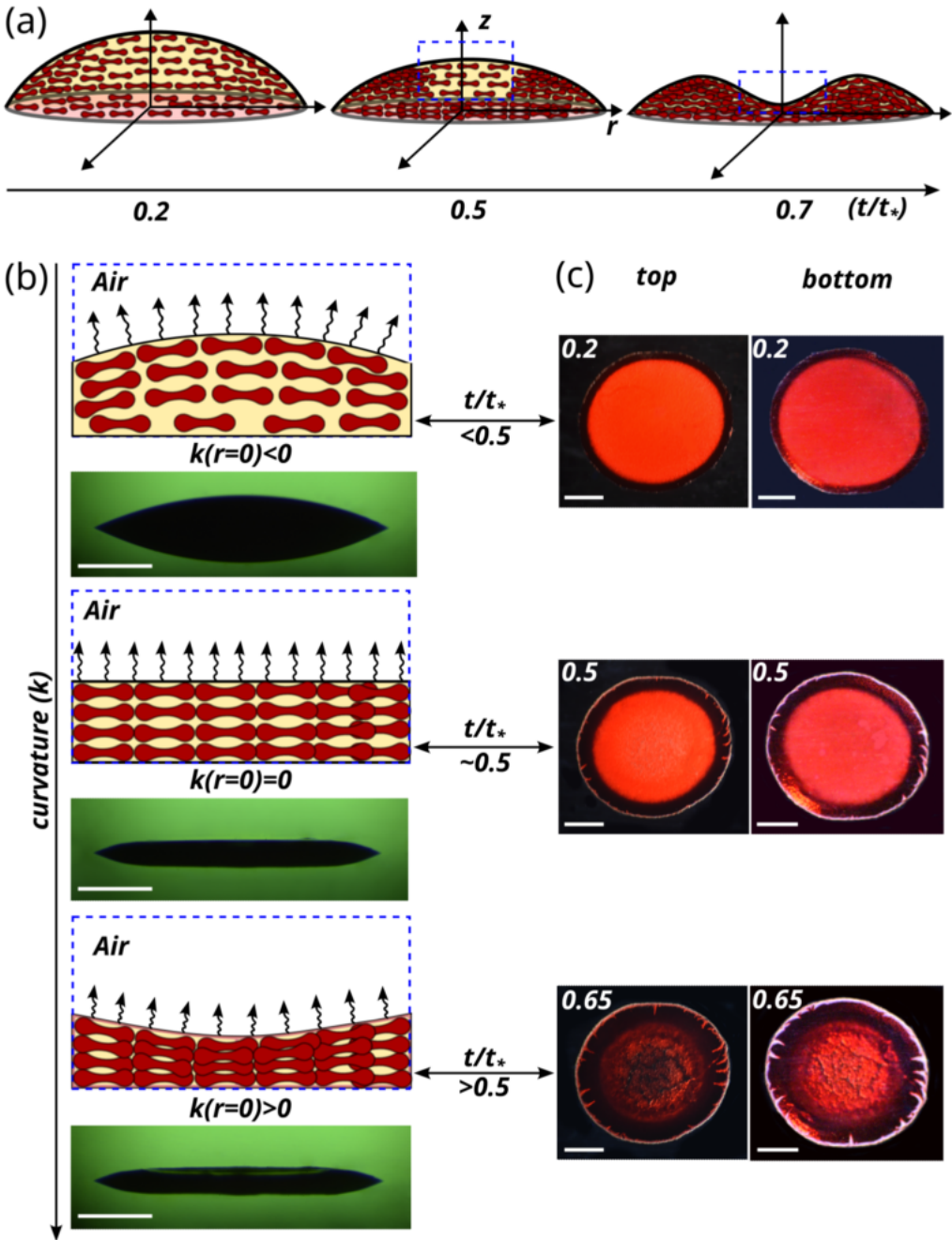


FIGURE 5. (a) 3D Schematic representation of blood droplet evaporation in Phase B from $t/t_* = 0.2 - 0.7$. (b) Schematic and side view data showing the curvature change at the drop center during evaporation process in Phase B for $t/t_* < 0.5$, $t/t_* \sim 0.5$, $t/t_* > 0.5$ respectively. The scale bar represents 1.3 mm respectively. (c) Top and bottom view image sequence corresponding to curvature evolution discussed in (b) at $t/t_* = 0.2, 0.5, 0.65$ respectively. The scale bar represents 1 mm respectively.

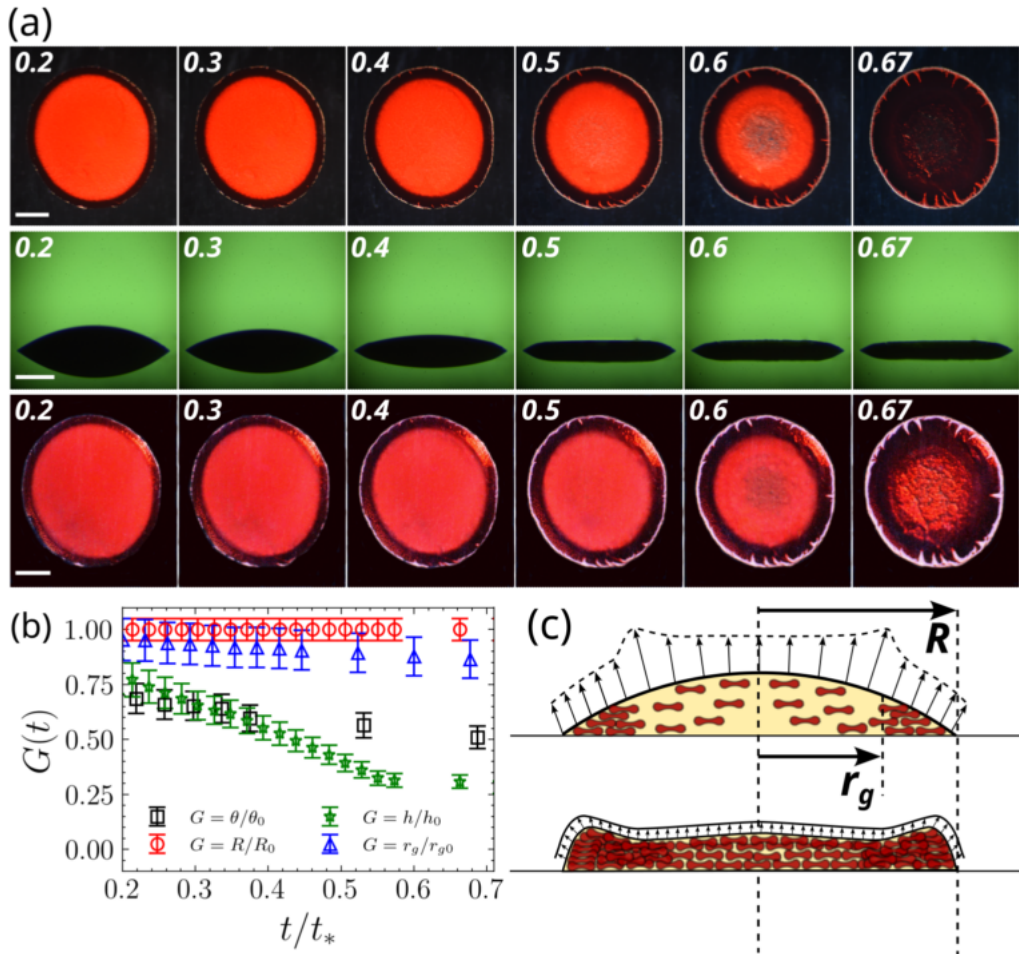


FIGURE 6. (a) Top, side and bottom view time sequence images of Phase B at various non dimensional time instants $t/t_* = 0.2, 0.3, 0.4, 0.5, 0.6, 0.67$ respectively. The Scale bar represents 1 mm. (b) Non dimensional geometrical drop parameters $G(t)$ (normalized contact angle (θ/θ_0), normalized drop height (h/h_0), normalized contact radius (R/R_0) and normalized gelation radius r_g/r_{g0}) evolution as a function of non dimensional time t/t_* . (c) Schematic representing the evaporating droplet at the beginning of phase B ($t/t_* = 0.2$) and end of phase B ($t/t_* \sim 0.67 - 0.7$) respectively.

of phase B, the entire droplet undergoes a sol-gel phase transition to a final wet gel form. The wet gel phase contains very small (trace) amounts of liquid water that evaporates in the next phase, C. We can also observe from the side view image panel that there is negligible change in droplet geometry, signifying the completion of gelation for the entire droplet.

3.3.3. Phase C

Figure 7 shows a schematic representation of phase C. Phase C is the final stage ($t/t_* = 0.7 - 1.0$) of the evaporation process with a very low evaporation rate. In this phase, the wet gel from the previous phase is further desiccated and transformed into a dry gel. Figure 7(a) shows a schematic of the wet and dry gel state. Figure 7(b) shows a typical side-view image during phase C of the evaporation process. Figure 7(c) depicts a

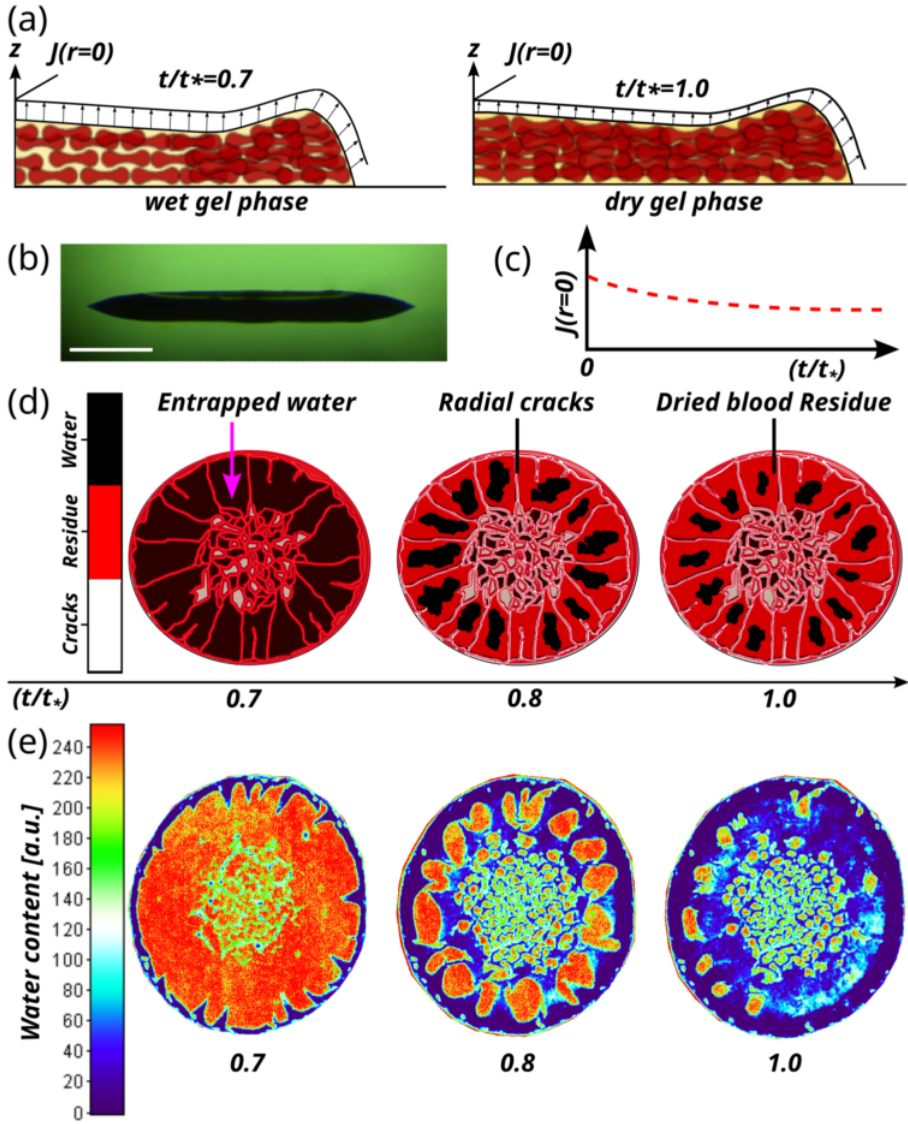


FIGURE 7. (a) Schematic of side view representing Phase C evaporation process depicting wet gel phase at $t/t_* = 0.7$, and dry gel phase at $t/t_* = 1.0$ respectively. (b) Typical side view during Phase C of the evaporation. The scale bar represents 1.3 mm. (c) Schematic representing the evaporation flux time evolution at the drop center. (d) Schematic of top view representing the evaporating drop in phase C ($t/t_* = 0.7 - 1.0$) depicting entrapped water, radial cracks, and dried blood residue. (e) Evolution of entrapped water evaporation as a function of non-dimensional time in phase C represented as an intensity color map.

slight reduction in evaporation flux as the solute concentration increases a little during desiccation in phase C. Figure 7(d) shows a schematic of the top view of the evaporating drop in phase C ($t/t_* = 0.7 - 1.0$) depicting the formation of radial cracks, shrinkage of trace amounts of water and dried blood residue. Figure 7(e) shows the evaporation of the entrapped water in the wet gel phase as a function of nondimensional time represented as an intensity color map in arbitrary units (a.u.) for effective visualization. Figure 8(a) shows the image sequence of the top, side, and bottom view of the desiccating

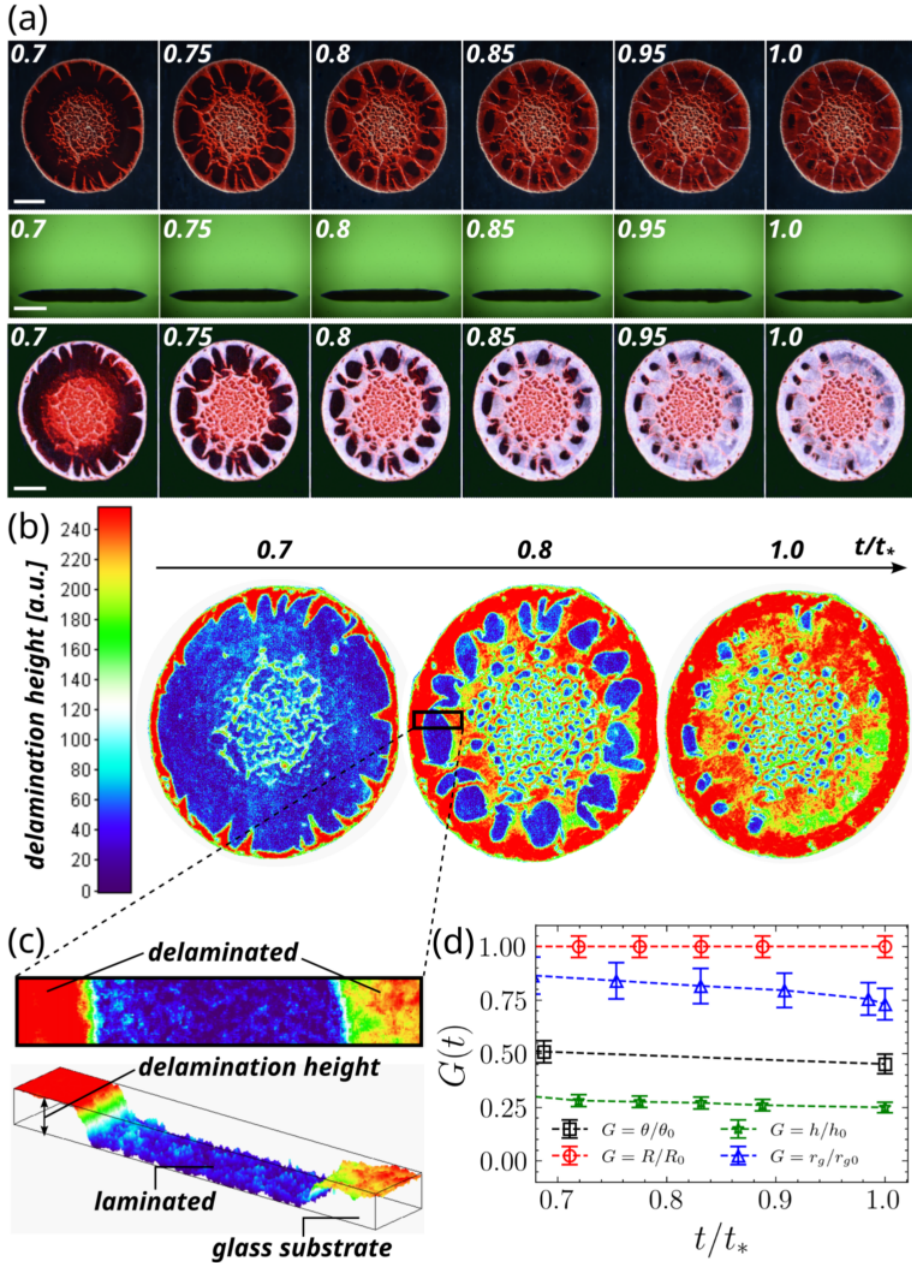


FIGURE 8. (a) Top, side and bottom view time sequence images of Phase C at non dimensional time instants $t/t_* = 0.7, 0.75, 0.8, 0.85, 0.95, 1.0$ respectively. The scale bar represents 1 mm. (b) Evolution of the 2D delamination height as a function of non-dimensional time in phase C represented as an intensity color map. (c) Magnified view depicting a typical laminated and delaminated region at the corona of dried blood residue at $t/t_* = 0.8$. (d) Non dimensional geometrical drop parameters $G(t)$ (normalized contact angle, normalized drop height, normalized contact radius and normalized gelation radius) evolution as a function of non dimensional time t/t_* .

drop, respectively. Notice the distinct color change in the top and bottom view as the drop transforms from wet gel to dry gel. From both the top and bottom view, we can observe the evaporation process of the trace amounts of water present at the beginning of phase C. Dessication stresses are developed as the drop undergoes further evaporation, forming various types of cracks. Radial cracks are observed in the thicker outer rim region, whereas mudflat cracks are observed in the center and the contact line region. Figure 8(b) denotes the time sequence of 2D delamination height represented as an intensity color map in arbitrary units (a.u.) during wet gel to dry gel transformation in Phase C. Figure 8(c) depicts a magnified view of the corona region of the dried blood precipitate highlighting regions like laminated and delaminated sections over the glass substrate. The dried residue undergoes a lamination-to-delamination transition as the wet gel transforms into a dry gel. The trace amounts of water present in the wet gel phase (red region in the intensity color map shown in figure 7(d) and 7(e)) cause the wet gel to adhere to the glass substrate (blue region in the intensity color map shown in figure 8(b) and 8(c)) due to the hydrophilic nature of glass substrate. However, on further desiccation, the water content in the laminated region decreases and leads to delamination from the substrate due to the phobic nature of the residual glycoproteins found on the surface of the RBCs (Brutin *et al.* 2011). The primary functionality of the glycoproteins is to minimize wettability from a surface. Figure 8(d) shows the slow variation of the nondimensional geometric parameters such as contact angle, drop center height, contact radius, and gelation radius as a function of nondimensional time. It is important to contrast the slow variation of the geometrical parameters in phase C from the relatively fast variation in phases A and B.

3.4. Generalized Mechanics of Blood drop evaporation

The initial capillary flow initiated due to the non uniform evaporation flux over the drop surface can be modelled using Stokes flow in cylindrical coordinates (refer to figure 2(a)). We follow the analysis of Brutin *et al.*, Tarasevich *et al.*, and Sobac *et al.* (Brutin *et al.* 2011; Tarasevich *et al.* 2011; Sobac & Brutin 2011) very closely for computing the dynamics of drop evaporation. From the radial component of the Stokes equation along with the thin film approximation (lubrication approximation) we have

$$\frac{\partial p}{\partial r} = \eta \frac{\partial^2 u}{\partial z^2} \quad (3.8)$$

From the axial component of the Stokes equation we have

$$\frac{\partial p}{\partial z} = 0 \quad (3.9)$$

where p is the pressure, r is the radial coordinate, η is the drop viscosity, u is the radial velocity, and z is the axial coordinate. Assuming cylindrical symmetry about the vertical axis, the continuity equation can be written as

$$\frac{1}{r} \frac{\partial(ru)}{\partial r} + \frac{\partial w}{\partial z} = 0 \quad (3.10)$$

The boundary condition for pressure field on the drop surface $z = h(r, t)$ is given by

$$p|_{z=h(r,t)} = -\sigma k \quad (3.11)$$

where σ is the surface tension and k is the curvature of the drop interface given by

$$k = \frac{1}{r} \frac{\partial}{\partial r} \left(r \frac{\partial h}{\partial r} \right) \quad (3.12)$$

Further, at the drop interface $z = h(r, t)$ we have

$$\left. \frac{\partial u}{\partial z} \right|_{z=h(r,t)} = 0 \quad (3.13)$$

owing to the fact that the radial velocity u has negligible variation in the axial direction z . The no slip and no penetration boundary condition at the surface of the substrate $z = 0$ ensures

$$u|_{z=0} = 0 \quad (3.14)$$

and

$$w|_{z=0} = 0 \quad (3.15)$$

Using equation (3.10) - (3.15) the radial velocity u can be written as

$$u = -\frac{\sigma}{\eta} \frac{\partial}{\partial r} \left(\frac{1}{r} \frac{\partial}{\partial r} \left(r \frac{\partial h}{\partial r} \right) \right) \left(\frac{z^2}{2} - hz \right) \quad (3.16)$$

The z component of fluid velocity is given by

$$w = \frac{\sigma}{r} \frac{\partial}{\partial r} \left(\frac{r}{\eta} \frac{\partial}{\partial r} \left(\frac{1}{r} \frac{\partial}{\partial r} \left(r \frac{\partial h}{\partial r} \right) \right) \left(\frac{z^3}{6} - h \frac{z^2}{2} \right) \right) \quad (3.17)$$

Integrating equation (3.16) with respect to z , the droplet height average radial velocity $\langle u \rangle$ is given as

$$\langle u \rangle = \frac{1}{h} \int_0^h u dz = \frac{h^2}{3} \frac{\sigma}{\eta} \frac{\partial}{\partial r} \left(\frac{1}{r} \frac{\partial}{\partial r} \left(r \frac{\partial h}{\partial r} \right) \right) \quad (3.18)$$

Using the continuity equation for the conservation of mass of the volatile component (here solvent majorly is the water content of the blood drop), the average radial velocity from equation (3.18), the dynamical equation for the drop height is given as

$$\frac{\partial h}{\partial t} = -\frac{1}{r} \frac{\partial (rh \langle u \rangle)}{\partial r} - \frac{J}{\rho} \quad (3.19)$$

where J is the evaporation flux and ρ is the density of the droplet. Similarly, using the continuity equation for the non-volatile component, i.e. solute (conservation of mass for the solute; here the major fraction of the), the dynamics of the height averaged solute concentration $\langle c \rangle$ is given as

$$\frac{\partial (h \langle c \rangle)}{\partial t} = -\frac{1}{r} \frac{\partial (rh \langle c \rangle \langle u \rangle)}{\partial r} \quad (3.20)$$

For small drop size where gravity is negligible compared to surface tension effects, the drop shape can be approximated by a spherical cap model. However the spherical cap model leads to singularities in the evaporation flux, flow velocity and solute concentration (RBCs here) near the contact line. As a result, we replace the initial drop shape by a paraboloid of revolution without the loss of generality as a initial condition. The initial drop shape is therefore given by

$$h|_{t=0} = h_f + h_0 \left(1 - \left(\frac{r}{R} \right)^2 \right) \quad (3.21)$$

where h_f is the drop height at the edge that corresponds to the precursor plasma film.

$$h|_{r=R} = h_f \quad (3.22)$$

The sum of h_f and h_0 represents the central drop height thickness, i.e., at $r = 0$. Owing to

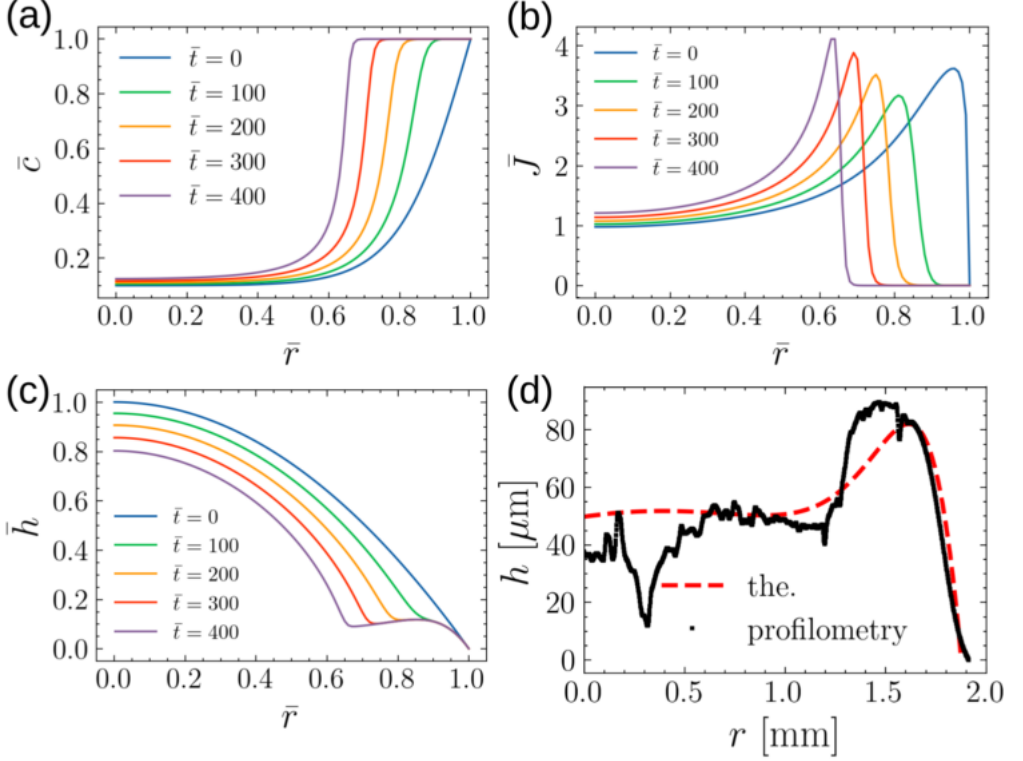


FIGURE 9. (a) Height averaged non dimensional concentration field plotted as a function of non dimensional radial coordinate at various non dimensional time instants $\bar{t} = 0, 100, 200, 300, 400$. (b) Non dimensional evaporation flux plotted as a function of non dimensional radial coordinate at various non dimensional time instants $\bar{t} = 0, 100, 200, 300, 400$. (c) Non dimensional drop height variation as a function of non dimensional radial coordinate at various non dimensional time instants $\bar{t} = 0, 100, 200, 300, 400$. (d) Theoretical and experimental comparison (profilometry) of dried blood droplet precipitate radial height profile.

the constant contact radius (CCR) mode of drop evaporation, the contact line of the drop is pinned and hence the radial velocity vanishes. The radial velocity also goes to zero at $r = 0$ due to vanishing curvature at the center. Therefore the boundary condition for the height average radial velocity $\langle u \rangle$ to solve equation (3.19) and (3.20) simultaneously is given by

$$\langle u \rangle|_{r=0} = \langle u \rangle|_{r=R} = 0 \quad (3.23)$$

The symmetry condition for the drop height profile gives

$$\left. \frac{\partial h}{\partial r} \right|_{r=0} = 0 \quad (3.24)$$

Similarly, the symmetry condition for the height averaged solute concentration is given by

$$\left. \frac{\partial \langle c \rangle}{\partial r} \right|_{r=0} = 0 \quad (3.25)$$

The initial height averaged solute concentration field is given by a known function $f(r)$ of radial coordinate

$$\langle c \rangle(r, 0) = f(r) \quad (3.26)$$

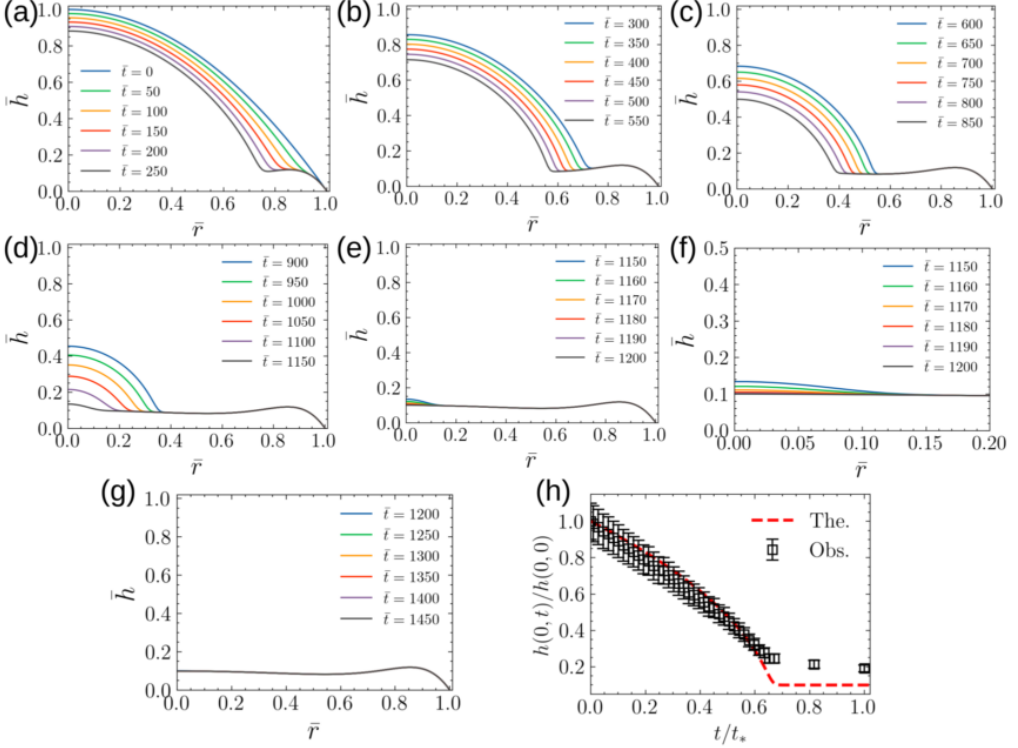


FIGURE 10. Non dimensional drop height variation as a function of non dimensional radial coordinate at various non dimensional time instants (a) $\bar{t} = 0 - 250$, (b) $\bar{t} = 300 - 550$, (c) $\bar{t} = 600 - 850$, (d) $\bar{t} = 900 - 1150$, (e) $\bar{t} = 1150 - 1200$, (f) magnified view of non dimensional height profile near $\bar{r} = 0 - 0.2$ for time instants $\bar{t} = 1150 - 1200$, (g) $\bar{t} = 1200 - 1450$. (h) Comparison of theoretical and experimental observation of drop center height variation with time.

We solve the equations for the drop height, solute concentration and evaporation flux in non-dimensional coordinate space. The drop height is normalized with respect to initial drop height h_0 as $h_f \ll h_0$, i.e., $\bar{h} = h/h_0$. The radial coordinate r is normalized with respect to drop contact radius R , i.e., $\bar{r} = r/R$. The height average radial velocity $\langle u \rangle$ is normalized with respect to the viscous velocity scale $u_c = \eta_0/\rho h_0$, i.e. $\bar{u} = \langle u \rangle / u_c$. Here η_0 is the viscosity of the solvent. The time scale t is normalized by a reference time scale R/u_c , i.e., $\bar{t} = tu_c/R$. The vapor flux J is normalized by a reference flux $J_c = k\Delta T/Lh_0$, i.e., $\bar{J} = J/J_c$; where k is the thermal conductivity of the liquid, ΔT is the difference between substrate and the saturation temperature and L is the latent heat of vaporization. The height averaged solute concentration $\langle c \rangle$ was normalized by the gelation concentration c_g , i.e., $\langle \bar{c} \rangle = \langle c \rangle / c_g$. Using the above normalized variables equation (3.19) and (3.20) can be non-dimensionalized and written as a vector equation with \bar{F} and \bar{f} expressed as a column vector

$$\frac{\partial \bar{F}}{\partial \bar{t}} + \bar{u} \frac{\partial \bar{F}}{\partial \bar{r}} = \bar{f} \quad (3.27)$$

where the column vectors \bar{F} and \bar{f} are given by

$$\bar{F} = \begin{bmatrix} \bar{h} \\ \langle \bar{c} \rangle \end{bmatrix} \quad (3.28)$$

and

$$\bar{f} = \left[-\frac{\bar{h}}{\bar{r}} \frac{\partial}{\partial \bar{r}} (\bar{r}\bar{u}) - E\bar{J} \right] \quad (3.29)$$

where

$$\bar{u} = \frac{\bar{h}^2}{3Ca} \frac{\partial}{\partial \bar{r}} \left(\frac{1}{\bar{r}} \frac{\partial}{\partial \bar{r}} \left(\bar{r} \frac{\partial h}{\partial \bar{r}} \right) \right) \quad (3.30)$$

Here $E = k\Delta T/\epsilon\eta_0L$ and $Ca = \eta u_c/\epsilon^3\sigma$ represents the evaporation and capillary number respectively, where $\epsilon = h_0/R$. The blood viscosity η dependence on the RBCs haematocrit Ht is given as (Lee Waite *et al.* 2007; Bergel 2012)

$$\eta = \eta_0 \left(\frac{1}{1 - \alpha Ht} \right) \quad (3.31)$$

where

$$\alpha = 0.076e^{2.49Ht+(1107/T)}e^{-1.69Ht} \quad (3.32)$$

and T is the temperature in Kelvin. The ratio of η/η_0 as a function of Ht is given in figure S4 of the supplementary material (refer to the supplementary). From the supplementary figure S4 it is evident that η increases monotonically with Ht . Ht physically represents the volume fraction of RBCs in the blood droplet. Therefore as the blood drop evaporates, Ht increases causing an equivalent increase in blood viscosity and capillary number Ca which further reduces the flow velocity scale \bar{u} inside the evaporating droplet, as $\bar{u} \propto Ca^{-1}$. The droplet precipitate thickness therefore becomes very weakly coupled to the flow velocity. The evaporative mass flux is modelled using techniques from heat transfer analysis (Anderson & Davis 1995) and also assuming that the vapor density vanishes at the sol-gel propagating front; i.e., the evaporative flux goes to zero as the concentration reaches a critical value of $\langle \bar{c} \rangle = 1$ ($\langle c \rangle = C_g$) during sol-gel phase transition at the propagating front. The dimensionless evaporation flux hence can be modeled as

$$\bar{J}(\bar{r}, \bar{t}) = \frac{1 - \langle \bar{c} \rangle^2}{k + \bar{h}} \quad (3.33)$$

where k is a dimensionless non equilibrium parameter. The range of k is such that $k \rightarrow \infty$ for non-volatile liquids and $k \rightarrow 0$ for volatile liquids. The initial condition for the nondimensional concentration profile required to solve equation (3.27) is given by

$$\langle \bar{c} \rangle(r, 0) = 2 - \bar{c}_0 + \frac{2(\bar{c}_0 - 1)}{1 + e^{w(\bar{r}-1)}} \quad (3.34)$$

where w is a measure of a characteristic length over which the concentration of colloidal particles increases rapidly. From the above distribution it is important to note that $\langle \bar{c} \rangle(0, 0) \simeq 0$ and $\langle \bar{c} \rangle(1, 0) = 1$ suggesting the initial concentration at the edge of the droplet is equal to the gelation concentration (gelation has already occurred at the three phase contact line). Using $D \sim 2.61 \times 10^{-5} \text{m}^2/\text{s}$, $c_v \sim 2.32 \times 10^{-2} \text{kg}/\text{m}^3$, $k \sim \mathcal{O}(1) \text{W}/\text{mK}$, $\Delta T \sim 75 \text{K}$, $\eta_0 \sim 5 \times 10^{-3} \text{Pa s}$, $L \sim 2.25 \times 10^6 \text{J}/\text{kg}$, $\epsilon \sim 0.4$, the system of differential equation for \bar{h} and $\langle \bar{c} \rangle$ given by equation (3.27) is computed using finite difference methods for $E \sim 10^{-2}$ and $Ca \sim 6 \times 10^{-5}$ corresponding to whole blood droplets used in our experiments.

Figure 9(a) shows the non dimensional average concentration profile for various non dimensional time instants $\bar{t} = 0, 100, 200, 300, 400$. Figure 9(b) shows the evolution of the evaporation flux profile along the drop interface for various non dimensional time instants $\bar{t} = 0, 100, 200, 300, 400$. Figure 9(c) shows the non dimensional drop height profile as a function of non dimensional radial coordinate with non dimensional time

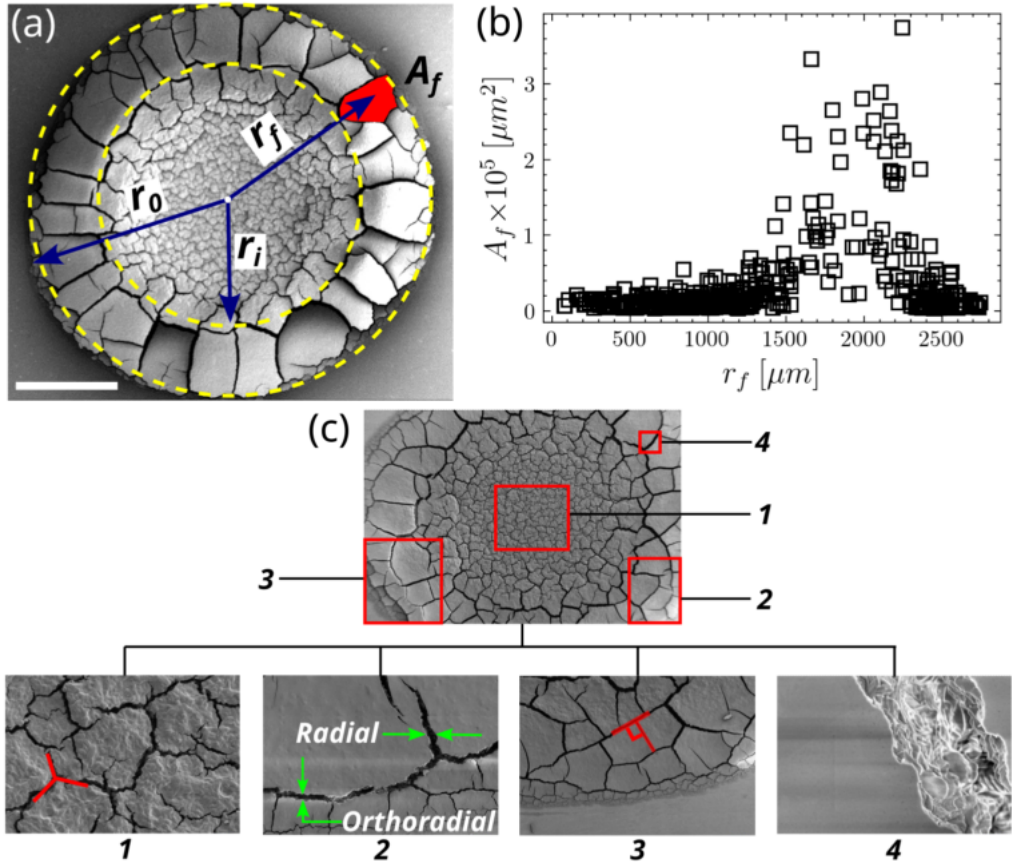


FIGURE 11. Dried blood precipitate characterization using (a) SEM denoting various kinds of cracks and flakes. Scale bar represents 1.3mm. (b) Radial flake size distribution of dried whole blood drop residue. (c) Cracks characterization in dried whole blood precipitate. The numerals 1-4 represents different viewing region of interest (ROI). 1, 2, 3, 4 represent the center, outer edge of the central region, peripheral region (corona) and a radial crack respectively.

as a parameter. Figure 9(d) compares the final dried residue droplet thickness profile with the steady state theoretical prediction. The theoretical height profile (red dotted line) conforms with the experimental curve obtained from profilometry (black) within the experimental uncertainty. Figure 10(a)-(g) shows the non dimensional height profile variation as a function of non dimensional radial coordinate with non dimensional time as a parameter in the range $\bar{t} = 0 - 1450$. Figure 10(h) shows the droplet center height variation as a function of non dimensional time t/t_* . The theoretical curve in red (labelled as The.) agrees with the experimental observations (labelled as Obs.) within the experimental uncertainty. The variation of the experimental observation from the theoretical prediction after $t/t_* = 0.7$ is due to the fact that the experimental drop center height data is extracted from the side view. As a result, after the reduction of the central height to approximately a particular value $(h(0, t)/h(0, 0) \sim 0.2)$, further reduction in the central height cannot be measured due to the formation of the thick coronal rim around the droplet. The coronal deposit obstructs the view of the center part of the droplet causing the measurement to flatten out much earlier compared to the actual theoretical prediction.

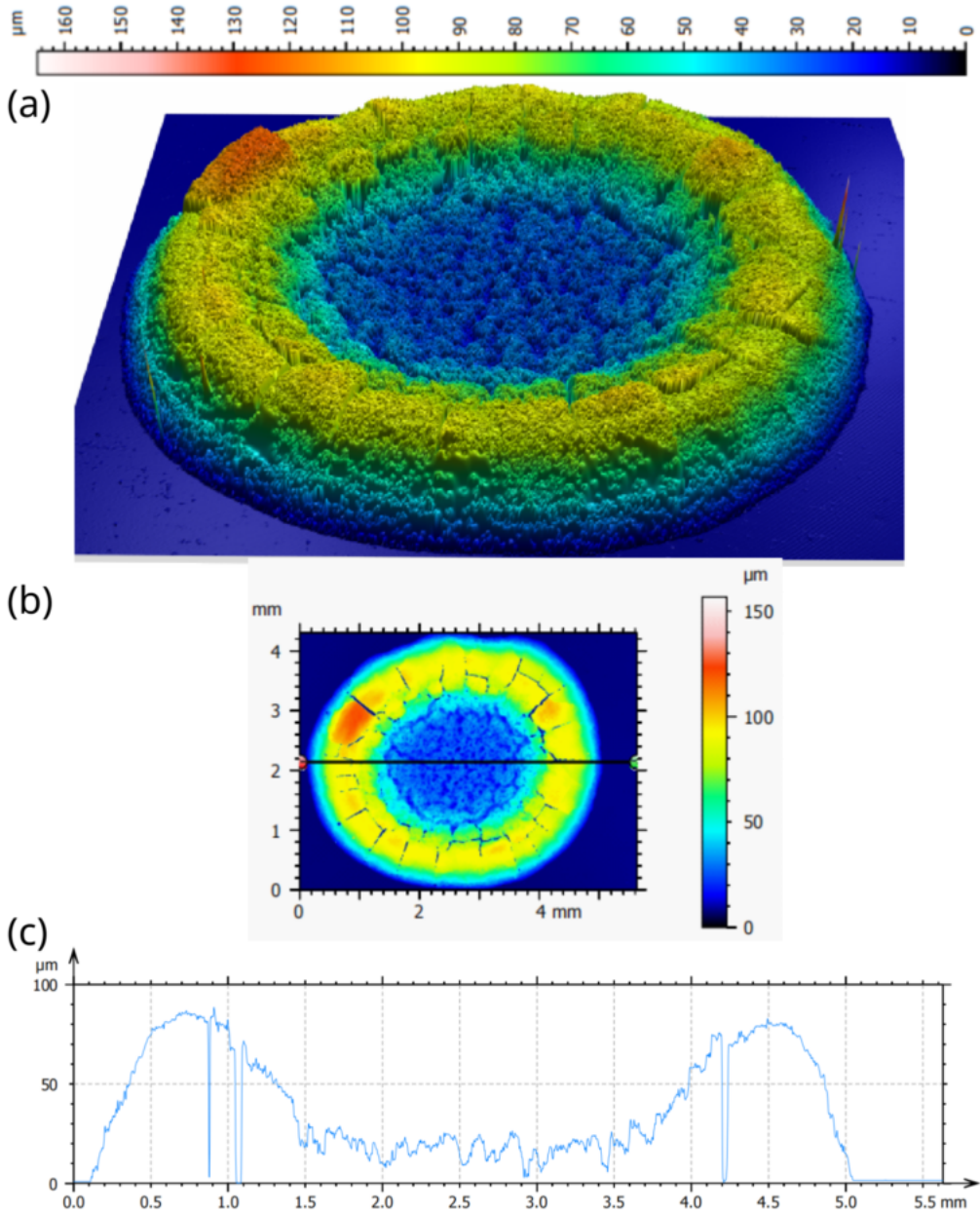


FIGURE 12. Dried blood drop surface thickness characterization using optical profilometry. (a) 3D perspective visualization of the dried residue surface and its corresponding thickness. (b) 2D visualization of dried precipitate surface thickness represented as a filled contour plot. (c) 1D surface profile thickness variation along the horizontal diametric axis (shown as black line in (b)) of the dried blood droplet precipitate.

3.5. Characterization of dried blood residues

Figure 11 (a) shows the SEM (scanning electron microscope) image of the dried residue of whole blood drop. The scale bar in white represents 1.3 mm. Various kinds of cracks are generally observed, ranging from radial cracks at the thickest portion to mudflat-type

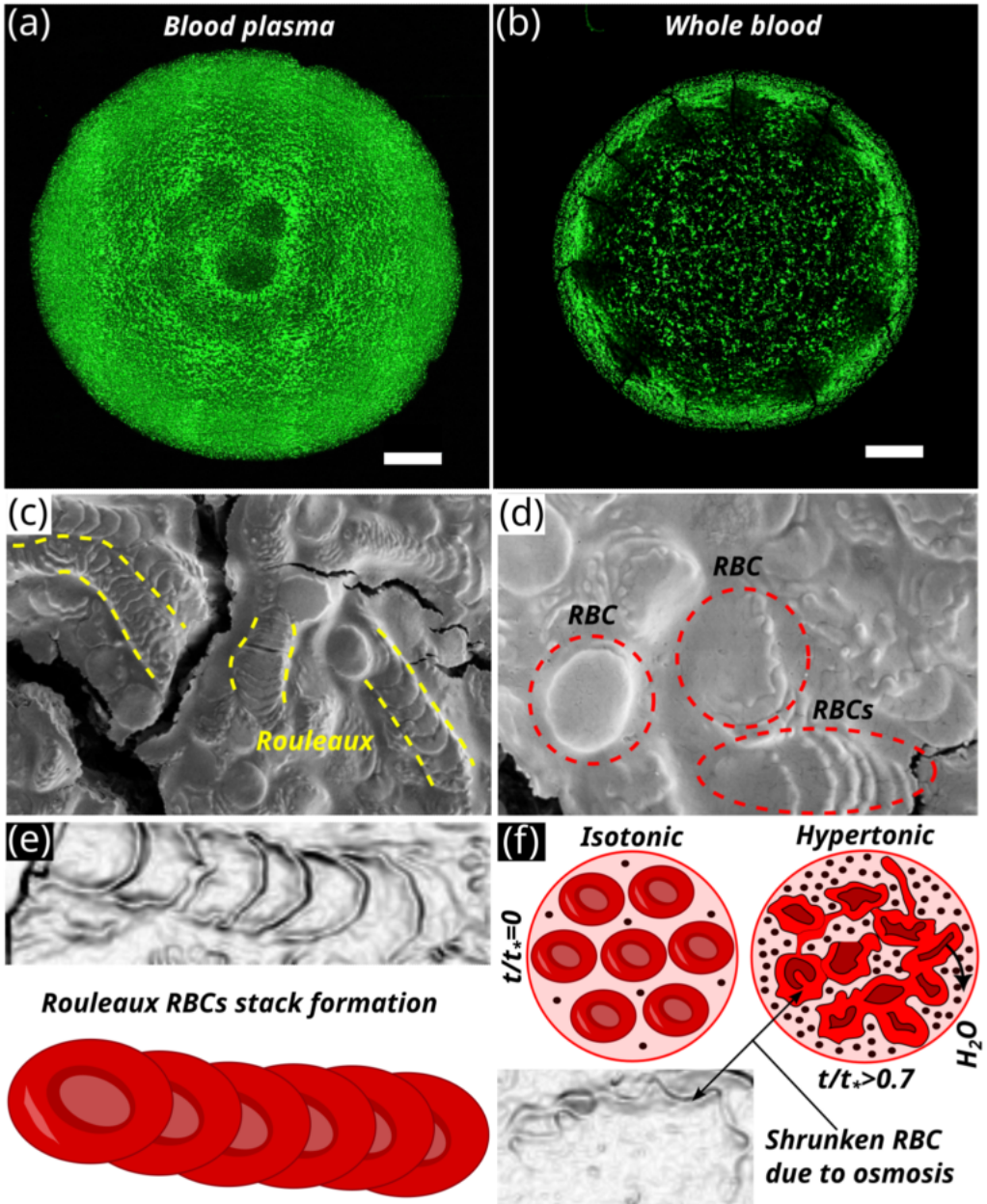


FIGURE 13. Confocal fluorescence microscopy images depicting bacterial distribution in the dried precipitate of (a) blood plasma and (b) Whole blood droplet. The white scale bar represents $500 \mu\text{m}$. (c) SEM image depicting RBCs distribution in the dried blood precipitate. (d) SEM image depicting shrunken RBCs. (e) Schematic representation of Rouleaux stack formation of RBCs. (f) Schematic representing osmosis in RBCs causing shape deformation from biconcave disk to shrunken state at the end state of evaporation (phase C).

cracks at the drop center and close to the droplet's outer edge. The cracks result from desiccation stress during the phase transition from wet to dry gel. Cracks, in general, intersect each other either at right angles or 120° . The resulting cracks fragment the dried residue into several flakes. Figure 11 (b) shows the radial size distribution of the flakes for a typical dried residue of contact radius $R = 2.7\text{mm}$. Here, A_f denotes the area of a particular flake with a radial centroid coordinate r_f , and R denotes the drop contact radius. The flake size is highest between $r_f = 1600 - 2300 \mu\text{m}$, i.e., in the peripheral region ($r_i = 1600 \mu\text{m}$, $r_0 = 2300 \mu\text{m}$). The flake size is smaller in the drop center and the outer edge of the droplet. Various regions of the dried residue can be characterized following Brutin et al. (Brutin *et al.* 2011). The region $0 < r < r_i$ refers to the central area of the drop, and the residue pattern is formed due to wetting deposits in general. The region $r_i < r < r_0$ forms the outer rim region called the corona. The deposition in the corona region is majorly due to the radially outward transport of RBCs due to the capillary flow inside the evaporating droplet. The outermost region $r_0 < r < R$ near the contact line of the drop has a deposit structure and crack morphology similar to the drop center formed due to wetting deposit. Figure 11(c) depicts the various cracks formed due to desiccation stress while transforming from wet gel to dry gel in phase C of blood drop evaporation. Different regions of interest in the dried residue are shown in red rectangles and labeled with 1-4 numerals. The central region labeled as 1 generally has mud-flat-type cracks. The cracks in the central region are typically shaped like "Y" at a vertex (intersection of cracks). Further, the cracks at a "Y" vertex typically subtend approximately equal angles close to 120° (figure 11 (c)-1). The cracks in the corona region labeled as 2 and 3 are typically "T" shaped and rectilinear. The cracks generally are radial and orthoradial (figure 11 (c)-2), intersecting at a right angle at the particular vertex (figure 11 (c)-3). The crack pattern of whole blood is drastically different from the crack pattern formed in pure blood plasma. Refer to supplementary figure S5 for the various types of crack formed in evaporating pure plasma drop. Figure 12 depicts a typical microcharacterization of the dried residue of whole blood using optical profilometry. Figure 12 (a) depicts a 3D visualization of the surface thickness profile for the dried blood precipitate. Note that the thickness of the dried precipitate is the smallest at the drop center and the outer contact line of the droplet. We observe that the crack thickness, length, and flake size at any given position are proportional to the thickness of the dried residue. Therefore, regions with higher thickness will have larger crack lengths and flake sizes. Physically, the crack length represents a scale over which the cracks form and stresses relax (Goehring 2013). Figure 12 (b) depicts the 2D thickness profile filled-contour corresponding to figure 12 (a). The 1D thickness profile along the section shown by black horizontal line (figure 12(b)) passing through the drop diameter is shown in figure 12 (c). We also observe that bacteria-laden blood droplets do not show a significant difference in terms of evaporation and dried residue characteristics from pure whole blood droplets within the concentration range typically found in living organisms $\sim \mathcal{O}(10 - 10^9)$ CFU/ml (refer to figure 2(b)). The negligible difference in drop evaporation and dried residue characteristics is probably due to RBCs being one order of magnitude ($\sim \mathcal{O}(10)$) bigger in length scale and hence approximately two order ($\sim \mathcal{O}(10^2)$) larger in terms of area ratio. The maximum bacterial concentration of 10^9 CFU/ml will give approximately similar number density as RBCs. However, owing to the area ratio, the bacteria will be uniformly distributed throughout the plasma protein matrix with the highest fraction embedded and packed between the biconcave curvatures of the RBCs. For bacteria to have appreciable effects in the corresponding evaporation physics, the packed cell volume (PCV) has to be significantly altered by the presence of bacteria. Alteration of PCV through bacteria is only possible at very high bacterial concentrations. The distribution of bacteria in the dried blood residue

can be seen from confocal microscopy and SEM of the dried residue, as shown in figure 13. Figures 13 (a) and 13 (b) depict the bacterial deposition in the dried residue of blood plasma and whole blood droplets using confocal fluorescence microscopy. The scale bar in white denotes $500\ \mu\text{m}$. Figure 13 (c-e) shows the RBCs' shape, deposition, and stacking in the dried blood residue using SEM. Generally, the RBCs stack in columnar structures known as rouleaux due to Smoluchowski aggregation/coagulation kinetics (Samsel & Perelson 1982, 1984; Barshtein *et al.* 2000). Due to the evaporation of blood droplets, the solute concentration increases. As a result, blood tonicity changes from isotonic to hypertonic, causing the RBCs to shrink in size due to water transport out of the red cells, as shown schematically in figure 13(f). The water transport outside the RBCs is caused by the osmotic pressure gradient, resulting in shrunken and wrinkled RBCs inside the precipitate of the evaporating droplet.

4. Conclusion

In conclusion, we study the mechanics of sessile whole blood drop evaporation using direct experimental visualization and theoretical methods like time sequence analysis, lubrication analysis, and micro/nano-characterization. We identified that blood drop evaporation, in general, can be subdivided into three phases (A, B, C) based on the evaporation rate. Phase A is the fastest and consists of the gelation of the contact line due to the radial transport of RBCs caused by the outward capillary flow. The gelation occurs due to sol-gel phase transition. Phase B consists of an intermediate evaporation rate in which the gelation front moves radially inward. The radially inward gelation front propagation and droplet height reduction cause the phase transition of the entire droplet into a wet gel state. The wet gel phase changes to a dry gel state in Phase C of droplet evaporation. We also observe lamination to delamination transition in phase C. Further, as the wet gel transitions to dry gel, the final dried residue precipitate undergoes desiccation induced stresses that lead to different kinds of cracks forming on the precipitate. The crack characteristics depend highly on the precipitate's local thickness; hence, a one-to-one map exists between precipitate thickness and the corresponding cracks that are formed. We also show that the drop evaporation rate and final dried precipitate pattern do not change appreciably within the parameter variation of the bacterial concentration typically found in bacterial infection of living organisms as the order of magnitude of the effective packed cell volume (PCV) remains approximately constant.

Supplementary Movie Captions

Movie 1: Supplementary movie depicting a sample top view. Recorded at 1 frames per 10 seconds, playback speed 10 frames per second.

Movie 2: Supplementary movie depicting a sample side view. Recorded at 1 frames per 10 seconds, playback speed 10 frames per second.

Movie 3: Supplementary movie depicting a sample bottom view. Recorded at 1 frames per 10 seconds, playback speed 10 frames per second.

Declaration of Interests

The authors declare no conflict of interest.

REFERENCES

- ADACHI, EIKI, DIMITROV, ANTONY S & NAGAYAMA, KUNIYUKI 1995 Stripe patterns formed on a glass surface during droplet evaporation. *Langmuir* **11** (4), 1057–1060.
- AGHARKAR, AMEY NITIN, HAJRA, DIPASREE, ROY, DURBAR, JAISWAL, VIVEK, KABI, PRASENJIT, CHAKRAVORTTY, DIPSHIKHA & BASU, SAPTARSHI 2024 Evaporation of bacteria-laden surrogate respiratory fluid droplets: On a hydrophilic substrate vs contact-free environment confers differential bacterial infectivity. *Physics of Fluids* **36** (3), 031912, arXiv: https://pubs.aip.org/aip/pof/article-pdf/doi/10.1063/5.0196219/19855755/031912_1.5.0196219.pdf.
- ALLAIN, C & LIMAT, L 1995 Regular patterns of cracks formed by directional drying of a colloidal suspension. *Physical review letters* **74** (15), 2981.
- ANDERSON, DM & DAVIS, SH 1995 The spreading of volatile liquid droplets on heated surfaces. *Physics of Fluids* **7** (2), 248–265.
- BAHMANI, LEILA, NEYSARI, MAHDI & MALEKI, MANIYA 2017 The study of drying and pattern formation of whole human blood drops and the effect of thalassaemia and neonatal jaundice on the patterns. *Colloids and Surfaces A: Physicochemical and Engineering Aspects* **513**, 66–75.
- BARSHTEIN, G, WAJNBUM, D & YEDGAR, S 2000 Kinetics of linear rouleaux formation studied by visual monitoring of red cell dynamic organization. *Biophysical journal* **78** (5), 2470–2474.
- BASKURT, OGUZ K & MEISELMAN, HERBERT J 2003 Blood rheology and hemodynamics. In *Seminars in thrombosis and hemostasis*, vol. 29, pp. 435–450. Copyright© 2003 by Thieme Medical Publishers, Inc., 333 Seventh Avenue, New York, NY 10017.
- BERGEL, DEREK HUGH 2012 *Cardiovascular fluid dynamics*. Elsevier.
- BRUTIN, DAVID 2015 *Droplet wetting and evaporation: from pure to complex fluids*. Academic Press.
- BRUTIN, DAVID, SOBAC, BENJAMIN, LOQUET, BORIS & SAMPOL, JOSÉ 2011 Pattern formation in drying drops of blood. *Journal of fluid mechanics* **667**, 85–95.
- CAMERON, JAMES M, BUTLER, HOLLY J, PALMER, DAVID S & BAKER, MATTHEW J 2018 Biofluid spectroscopic disease diagnostics: A review on the processes and spectral impact of drying. *Journal of biophotonics* **11** (4), e201700299.
- CHEN, RUOYANG, ZHANG, LIYUAN, ZANG, DUYANG & SHEN, WEI 2016 Blood drop patterns: Formation and applications. *Advances in colloid and interface science* **231**, 1–14.
- CHOI, JUNHEE, KIM, WONJUNG & KIM, HO-YOUNG 2020 Crack density in bloodstains. *Soft Matter* **16** (24), 5571–5576.
- CLIFT, ROLAND, GRACE, JOHN R & WEBER, MARTIN E 2005 Bubbles, drops, and particles .
- DEEGAN, ROBERT D, BAKAJIN, OLGICA, DUPONT, TODD F, HUBER, GREG, NAGEL, SIDNEY R & WITTEN, THOMAS A 1997 Capillary flow as the cause of ring stains from dried liquid drops. *Nature* **389** (6653), 827–829.
- DEEGAN, ROBERT D, BAKAJIN, OLGICA, DUPONT, TODD F, HUBER, GREG, NAGEL, SIDNEY R & WITTEN, THOMAS A 2000 Contact line deposits in an evaporating drop. *Physical review E* **62** (1), 756.
- DEMIR, RAMIZ, KOC, SONER, OZTURK, DENIZ GULFEM, BILIR, SUKRIYE, OZATA, HALIL İBRAHİM, WILLIAMS, RHODRI, CHRISTY, JOHN, AKKOC, YUNUS, TINAY, İLKER, GUNDUZ-DEMİR, CIGDEM & OTHERS 2024 Artificial intelligence assisted patient blood and urine droplet pattern analysis for non-invasive and accurate diagnosis of bladder cancer. *Scientific Reports* **14** (1), 2488.
- DENKOV, N, VELEV, O, KRALCHEVSKI, P, IVANOV, I, YOSHIMURA, HIDEYUKI & NAGAYAMA, KUNIYUKI 1992 Mechanism of formation of two-dimensional crystals from latex particles on substrates. *Langmuir* **8** (12), 3183–3190.
- DUFRESNE, ERIC I, CORWIN, ERIC I, GREENBLATT, NA, ASHMORE, JACQUELINE, WANG, DY, DINSMORE, ANTHONY D, CHENG, JX, XIE, XS, HUTCHINSON, JOHN W & WEITZ, DAVID A 2003 Flow and fracture in drying nanoparticle suspensions. *Physical review letters* **91** (22), 224501.
- ESMONDE-WHITE, KAREN A, ESMONDE-WHITE, FRANCIS WL, MORRIS, MICHAEL D & ROESSLER, BLAKE J 2014 Characterization of biofluids prepared by sessile drop formation. *Analyt* **139** (11), 2734–2741.

- GENNES, PIERRE-GILLES, BROCHARD-WYART, FRANÇOISE, QUÉRÉ, DAVID & OTHERS 2004 *Capillarity and wetting phenomena: drops, bubbles, pearls, waves*. Springer.
- GOEHRING, LUCAS 2013 Evolving fracture patterns: columnar joints, mud cracks and polygonal terrain. *Philosophical Transactions of the Royal Society A: Mathematical, Physical and Engineering Sciences* **371** (2004), 20120353.
- HERTAEG, MICHAEL J, TABOR, RICO F, ROUTH, ALEXANDER F & GARNIER, GIL 2021 Pattern formation in drying blood drops. *Philosophical Transactions of the Royal Society A* **379** (2203), 20200391.
- HOFFBRAND, VICTOR & STEENSMA, DAVID P 2019 *Hoffbrand's essential haematology*. John Wiley & Sons.
- HU, HUA & LARSON, RONALD G 2002 Evaporation of a sessile droplet on a substrate. *The Journal of Physical Chemistry B* **106** (6), 1334–1344.
- HU, HUA & LARSON, RONALD G 2005 Analysis of the microfluid flow in an evaporating sessile droplet. *Langmuir* **21** (9), 3963–3971.
- IQBAL, R, SHEN, AMY Q & SEN, AK 2020 Understanding of the role of dilution on evaporative deposition patterns of blood droplets over hydrophilic and hydrophobic substrates. *Journal of Colloid and Interface Science* **579**, 541–550.
- ISRAELACHVILI, JACOB N 2011 *Intermolecular and surface forces*. Academic press.
- KOKORNACZYK, MARIA OLGA, BODROVA, NATALIA BORISOVNA & BAUMGARTNER, STEPHAN 2021 Diagnostic tests based on pattern formation in drying body fluids—a mapping review. *Colloids and Surfaces B: Biointerfaces* **208**, 112092.
- LANOTTE, LUCA, LAUX, DIDIER, CHARLOT, BENOÎT & ABKARIAN, MANOUK 2017 Role of red cells and plasma composition on blood sessile droplet evaporation. *Physical Review E* **96** (5), 053114.
- LAUX, D, FERRANDIS, JY & BRUTIN, DAVID 2016 Ultrasonic monitoring of droplets' evaporation: Application to human whole blood. *Ultrasonics Sonochemistry* **32**, 132–136.
- LEE WAITE, PH, FINE, JERRY & OTHERS 2007 *Applied biofluid mechanics*. The McGraw-Hill Medical Companies, Inc.
- MUKHOPADHYAY, MANIKUNTALA, RAY, RUDRA, AYUSHMAN, MANISH, SOOD, POURUSH, BHATTACHARYYA, MAITREYEE, SARKAR, DEBASISH & DASGUPTA, SUNANDO 2020 Interfacial energy driven distinctive pattern formation during the drying of blood droplets. *Journal of Colloid and Interface Science* **573**, 307–316.
- NGUYEN, VAN X & STEBE, KATHLEEN J 2002 Patterning of small particles by a surfactant-enhanced marangoni-bénard instability. *Physical Review Letters* **88** (16), 164501.
- PAL, ANUSUYA, GOPE, AMALESH & SENGUPTA, ANUPAM 2023 Drying of bio-colloidal sessile droplets: Advances, applications, and perspectives. *Advances in Colloid and Interface Science* **314**, 102870.
- REINHART, WALTER H 2016 The optimum hematocrit. *Clinical hemorheology and microcirculation* **64** (4), 575–585.
- SAMSEL, RW & PERELSON, AS 1984 Kinetics of rouleau formation. ii. reversible reactions. *Biophysical journal* **45** (4), 805–824.
- SAMSEL, RICHARD W & PERELSON, ALAN S 1982 Kinetics of rouleau formation. i. a mass action approach with geometric features. *Biophysical Journal* **37** (2), 493–514.
- SCHNEIDER, CAROLINE A, RASBAND, WAYNE S & ELICEIRI, KEVIN W 2012 Nih image to imagej: 25 years of image analysis. *Nature methods* **9** (7), 671–675.
- SHATOKHINA, SN, SHABALIN, VN, BUZOVERYA, ME, PUNIN, VT & OTHERS 2004 Bio-liquid morphological analysis. *The Scientific World Journal* **4**, 657–661.
- SMALYUKH, IVAN I, ZRIBI, OLENA V, BUTLER, JOHN C, LAVRETOVICH, OLEG D & WONG, GERARD CL 2006 Structure and dynamics of liquid crystalline pattern formation in drying droplets of dna. *Physical review letters* **96** (17), 177801.
- SOBAC, BENJAMIN & BRUTIN, DAVID 2011 Structural and evaporative evolutions in desiccating sessile drops of blood. *Physical Review E* **84** (1), 011603.
- TARASEVICH, YURI YU, VODOLAZSKAYA, IRINA V & ISAKOVA, OLGA P 2011 Desiccating colloidal sessile drop: dynamics of shape and concentration. *Colloid and Polymer Science* **289**, 1015–1023.
- TRAIPE-CASTRO, LEONIDAS, SALINAS-TORO, DANIELA, LÓPEZ, DANIELA, ZANOLLI, MARIO, SRUR, MIGUEL, VALENZUELA, FELIPE, CÁCERES, ANÍBAL, TOLEDO-ARAYA, HÉCTOR &

- LÓPEZ-SOLÍS, REMIGIO 2014 Dynamics of tear fluid desiccation on a glass surface: a contribution to tear quality assessment. *Biological Research* **47**, 1–10.
- VAN ROSSUM, G & DRAKE, FL 2009 Python 3 reference manual createspace. *Scotts Valley, CA*
- WILKING, JAMES N, ZABURDAEV, VASILY, DE VOLDER, MICHAEL, LOSICK, RICHARD, BRENNER, MICHAEL P & WEITZ, DAVID A 2013 Liquid transport facilitated by channels in bacillus subtilis biofilms. *Proceedings of the National Academy of Sciences* **110** (3), 848–852.
- WILSON, ANDREW S, BROWN, EMMA L, VILLA, CHIARA, LYNNERUP, NIELS, HEALEY, ANDREW, CERUTI, MARIA CONSTANZA, REINHARD, JOHAN, PREVIGLIANO, CARLOS H, ARAOZ, FACUNDO ARIAS, GONZALEZ DIEZ, JOSEFINA & OTHERS 2013 Archaeological, radiological, and biological evidence offer insight into inca child sacrifice. *Proceedings of the National Academy of Sciences* **110** (33), 13322–13327.
- WILSON, STEPHEN K & D'AMBROSIO, HANNAH-MAY 2023 Evaporation of sessile droplets. *Annual Review of Fluid Mechanics* **55**, 481–509.
- YAKHNO, TATIANA A, SANIN, ANATOLY G, YAKHNO, VLADIMIR G, PELYUSHENKO, ARTEM S, DOWELL, MICHAEL B, VACCA, CHRISTINA & GOUTOROVA, VALENTINA A 2005 Drying drops of biological liquids: dynamics of the optical and mechanical properties. application in rapid medical diagnostics. In *Advanced Biomedical and Clinical Diagnostic Systems III*, , vol. 5692, pp. 188–198. SPIE.